Precise tuning of the thickness and optical properties of highly stable 2D organometal halide perovskite nanosheets through a solvothermal process and its applications as a white LED and a fast photodetector

Sumaiya Parveen[1], Kamal Kumar Paul[1], and P. K. Giri[1, 2*]

[1]Department of Physics, Indian Institute of Technology Guwahati, Guwahati -781039, India

[2]Centre for Nanotechnology, Indian Institute of Technology Guwahati, Guwahati -781039, India

Keywords: *2D perovskite nanosheet; layer control; Fast solvothermal process; photoluminescence quantum yield; fast response photodetector; stability*

Abstract

Precise control of the thickness of large-area 2D organometal halide perovskite layers is extremely challenging owing to the inherent instability of the organic component. Herein, a novel, highly reproducible and facile solvothermal route is reported to synthesize and tailor the thickness and optical bandgap of the organic-inorganic halide perovskite nanosheets (NS). Our study reveals that self-assembly of randomly oriented perovskite nanorods leads to the growth of multilayered perovskite NS at ~100 °C, while at higher temperature large area few-layer to bilayer 2D NS ($CH_3NH_3PbBr_3$) are obtained through lattice expansion and layer separation depending precisely on the temperature. Interestingly, the thickness of the 2D NS shows a linear dependence on the reaction temperature and thus enables precise tuning of the thickness from 14 layers to 2 layers giving rise to a systematic increase in the bandgap and appearance

* Corresponding author, email: giri@iitg.ac.in

of excitonic absorption bands. Quantitative analysis of the change in the bandgap with thickness revealed strong quantum confinement effect in the 2D layers. The perovskite 2D NS exhibits tunable color and high photoluminescence (PL) quantum yields (QY) up to 84 %. Through a careful analysis of the steady-state and time-resolved PL spectra, the origin of the lower PL QY in thinner NS is traced to surface defects in the 2D layers, for the first time. A white light converter was fabricated using the composition tuned 2D $CH_3NH_3PbBrI_2$ NS on a blue LED chip. The 2D perovskite photodetector exhibits a stable and very fast rise/fall time (24 μs/103 μs) along with high responsivity and detectivity of ~1.93 A/W and 1.04×10^{12} Jones, respectively. Storage, operational and temperature dependent stability studies reveal high stability of the 2D perovskite NS under the ambient condition with high humidity. The reported method is highly promising for the development of large-area stable 2D perovskite layers for various cutting-edge optoelectronic applications.

1. Introduction

Low dimensional organic-inorganic halide perovskites nanostructures have recently aroused a great deal of interest due to their low cost, easy solution processing, good stability, and outstanding optoelectronic properties.[1-8] Intensive research is being conducted especially on 2D nanoplatelet or nanosheet (NS) in comparison to their bulk, 1D and 0D counterparts for its appealing features, such as large lateral size, narrow band absorption and emission spectra, long diffusion length and long carrier lifetime, excellent charge transport properties, which makes it a promising material for the applications in photovoltaics and optoelectronics.[9-18] Interestingly, organic-inorganic halide perovskite ($MAPbBr_3$, MA= CH_3NH_3) nanocrystals (NCs) have gained more attention and are widely used in various devices as compared to the inorganic $CsPbBr_3$ or $FAPbBr_3$, since it can be synthesized at room temperature with low cost due to its low formation energy.[19-21]

In the literature, very few reports have addressed on the synthesis of colloidal 2D organic-inorganic halide perovskite nanoplatelets due to lack of control in the growth of pure 2D NSs.[10, 12, 15, 22] Gonzalez-Carrero et al. prepared a blue luminescent 2D perovskite using $C_{18}H_{40}BrN$ as the organic component.[23] Dou et al. used $C_4H_{11}NHBr$ and CH_3NH_3Br for the growth of single- and few-unit-cell-thick single-crystalline 2D hybrid perovskites of $(C_4H_9NH_3)_2PbBr_4$.[24] Sichert et al. tuned the thickness and photoluminescence properties of the perovskite by varying the ratio of organic cations (CH_3NH_3Br and $C_{32}H_{68}BrN$).[10] Cho et al. modulated the layer thickness of the perovskite nanoplatelet by changing the chain length and concentration of the added alkylammonium cations.[12] Similarly, Yuan et al. used different organic ammonium bromide salts to tune the color of highly luminescent quasi-2D layered structured perovskite ($(C_6H_5CH_2NH_3)_2PbBr_4$).[22] Levchuk et al. realized the thickness-tunability of perovskite nanoplatelet using the ligand-assisted re-precipitation method by varying the oleylamine and oleic acid ligand ratio.[15] In these reports, different kinds of organic amine salts and different ratios of capping ligands have been used to tune the thickness of the 2D perovskite. However, precise tuning of the thickness of 2D layer through temperature control and the long term stability of the 2D layer are least addressed in the literature, and such control is highly desirable for its exploitation in demanding applications.

Interestingly, the solvothermal method is a very easy and facile route to tune the morphology of NSs due to the high pressure/temperature inside the closed environment of the autoclave. Although plenty of works have been done on tuning the morphology of the inorganic based perovskites ($CsPbBr_3$) using the solvothermal method, there is hardly any report on the effect of solvothermal treatment on the morphology of the organic-inorganic halide perovskites.[25-34] Zhang et al. demonstrated the preparation of mixed halide perovskite $CH_3NH_3Pb(Br_{1-x}Cl_x)_3$ single crystals by the solvothermal growth of stoichiometric $PbBr_2$ and $[(1-y)CH_3NH_3Br+yCH_3NH_3Cl]$ DMF precursor solutions.[26] Xia et a. developed a

hydrothermal method using $Pb(CH_3COO)_2.3H_2O$, HBr and CH_3NH_2 alcohol solution to prepare $CH_3NH_3PbBr_3$ cluster, which was used as active material in lithium batteries.[29] Recently, Zhang et al. fabricated hybrid materials via the encapsulation of perovskite $MAPbBr_3$ NCs in europium-based metal-organic frameworks, which has been used in multistage anti-counterfeiting.[25] Note that all the reported solvothermal methods required a long duration (12-48 hrs) of synthesis, which is not time and cost-efficient. In the literature, tuning of the thickness or optical properties of the nanoplatelet is achieved mostly by varying the number of ligands or organic salts. In contrast, we achieve highly tunable thickness and optical properties of the organic-inorganic halide perovskite through a short duration solvothermal method of reaction simply by controlling the growth temperature.

Herein, we demonstrate a facile, fast, controlled solvothermal method to tailor the thickness of the ultra-stable organic-inorganic halide perovskite ($MAPbBr_3$) NS with excellent tunable light absorption/ emission and photodetector performance. Transmission electron microscope (TEM) imaging at different stages of the synthesis allows us to monitor the shape evolution of the self-assembled NSs from nanorods (NRs) to NS to quantum dots (QDs) with increasing reaction temperature. Precise tuning of the thickness of the NSs from few layers to bilayer is evidenced from atomic force microscopy (AFM) height profile analysis. The growth mechanism of the NSs is qualitatively discussed based on the classical theory. Through the control of the thickness of the 2D NS, bandgap tuning is achieved from green luminescent NRs to cyan luminescent QDs. Simply by varying the growth temperature, a systematic blue shift in UV-Vis absorption edge and photoluminescence (PL) peak position is observed due to the quantum confinement (QC) effect. We demonstrate a high PL quantum yield (QY) (~78 %) for ~8.4 nm thick perovskite NSs with a sharp PL peak at ~518 nm, which is quite significant for the 2D NS. The prepared NS shows extremely high stability in ambient condition with high humidity. Uniformly distributed bright blue luminescent QDs with

extremely high PL QY also synthesized by increasing the Oleylamine (OAm) concentration. The real-life application of the 2D NSs was demonstrated by fabricating a white LED device by depositing the orange emitting $CH_3NH_3PbBr_1I_2$ NS on a blue LED. We also fabricate a photodetector device using the 2D perovskite NS that shows very high stability, fast response time and high responsivity. The efficacy of the current solvothermal method for fast, convenient and controllable synthesis of the large area, stable 2D perovskite layers and their uses in various optoelectronic devices are demonstrated here.

2. Experimental procedure

2.1. Materials

The starting materials for the present synthesis are methylamine solution (CH_3NH_3, 33 wt % in absolute ethanol, Sigma-Aldrich), lead(II) iodide (PbI_2, 99%, Sigma-Aldrich), lead(II) bromide ($PbBr_2$, 99.999%, Sigma-Aldrich), hydroiodic acid (HI, 57 wt % in water, Sigma-Aldrich), hydrobromic acid (HBr, 48 wt % in water, Sigma-Aldrich), N,N-dimethylformamide (DMF, >99%, Sigma-Aldrich), diethyl ether (>99%, Merck), toluene (Merk), Oleic acid ($CH_3(CH_2)_7CH=CH(CH_2)_7COOH$, Merk), Oleylamine (≥98% (primary amine), Sigma-Aldrich).

2.2. Synthesis procedures

2.2.1. Synthesis of CH_3NH_3Br

CH_3NH_3Br (MABr) powder was prepared by diluting the 8 mL of CH_3NH_3 solution with 50 mL of absolute ethanol while stirring the solution for 15 min in a round-bottom flask. Then, 2.83 mL HBr was slowly added to the solution in an ice bath with vigorous stirring at 900 rpm for 2 h. The solution was then heated at 70 °C for several hours with continuous stirring till the solvent evaporates. To remove impurities from the MABr powder and as well

as to recrystallize it, the powder was washed several times with anhydrous diethyl ether and finally dried at 60 °C in a vacuum oven overnight.

2.2.2. Synthesis of ultrathin 2D perovskite NS

To prepare the precursor solution, MABr and $PbBr_2$ were first mixed in DMF, and then Oleic acid was added to the solution. Next, 60 µl OAm was added to the solution and transferred it into a Teflon lined autoclave without any pretreatment and heated it at different temperatures (60°-180° C) for only 30 min. The synthesis procedure is presented in a schematic illustration in Scheme 1 (ESI). Note that reported solvothermal methods usually adopted long-duration reactions (12-48 hrs), in contrast to our fast reaction method. After the solvothermal process, the crude solution was cooled down naturally, and 400 µl of the solution was added into 10 ml toluene. The as-prepared NSs were separated from the solution by centrifugation for 15000 rpm for 15 min. The supernatant was discarded, and the precipitate was redispersed in 5 ml toluene for further characterization. No additional washing was adopted for purification. The samples are named as PB60, PB100, PB120, etc. according to the reaction temperatures, as detailed in Table 1. To prepare the $MAPbCl_3$, $MAPbI_3$, and mixed halide NSs, the same protocol was followed by replacing the $PbBr_2$ with $PbCl_2$, PbI_2 or mixed halide precursors (i.e., $PbCl_2$/$PbBr_2$ and PbI_2/$PbBr_2$), respectively. To illustrate the robustness of the method and the stability of the 2D perovskites, all the syntheses were carried out in ambient air with relatively high humidity (~70%) without the use of a glove box.

2.2.3. Fabrication of photodetector

First, Si/SiO_2 (300 nm) substrates were cleaned by ultra-sonication using acetone, iso-propanol, water sequentially each for 10 min, followed by drying/heating at 150 ºC for 1 h on the hot plate. The substrate was then treated by UV-Ozone for 20 min to remove any residue. To avoid the degradation of the material while depositing the electrodes, the Al electrodes were first deposited on the wafers using a shadow mask by a thermal evaporation method. Then the

PB140 NS solution was drop cast between the gap of two electrodes and dried at 60 ºC. We use a planar geometry of the device for simplicity of fabrication.

2.3. Characterization techniques

The morphology of perovskite NSs has been characterized using a FESEM (Sigma, Zeiss). The high magnification surface morphologies for different samples have been studied using a transmission electron microscope (TEM) (JEOL-JEM 2010) operated at 200 kV. AFM (Cypher, Oxford Instruments) images were acquired to find the thickness of the perovskite NSs. UV-Vis absorption spectra of the samples were measured using a commercial spectrophotometer (PerkinElmer, Lamda 950). The room temperature steady-state PL spectra were recorded using a commercial fluorimeter with 400 nm excitation using a Xenon lamp (Fluoromax-4, Horiba Scientific). PL QY of the samples was measured in a solution using an integrating sphere (FM-SPHERE, Horiba) attached with the fluorimeter. Low temperature (80–300 K) PL measurements were carried out using a liquid nitrogen-cooled optical cryostat (Optistat DNV, Oxford Instruments) attached to the above fluorimeter using 405 nm laser excitation. TRPL measurements were performed using a 405 nm pulsed laser excitation for perovskite NSs, with an instrument response time of <50 ps (LifeSpecII, Edinburgh Instruments). Photodetector measurement was carried out using an assembled setup consisting of a microprobe station (Ecopia, Korea), a 405 nm diode laser, a source meter (Keithley 2400, Germany), a pulse generator (Agilent) and a digital oscilloscope (Agilent). The spectral response and external quantum efficiency were measured using a 150 W Xe lamp (Newport, USA), a monochromator (Newport, USA) and a power meter (Newport, USA).

3. Results and discussions

3.1. Morphology and microstructural analysis

A schematic illustration of the synthesis procedure and the structural evolution of perovskite NSs with the variation of the solvothermal temperature (T_s) are depicted in Scheme 1 (electronic supporting information, ESI). Here, the solvothermal synthesis process is conducted inside an autoclave, which is placed inside a preheated oven and the reaction is initiated soon after the autoclave is placed inside the oven. Pressure in the liquid inside the close chamber is moderate to high, which favors the crystal nucleation while the surfactant is adsorbed onto the sidewalls of the autoclave, preventing the agglomeration of NS[35]. Figure S1 (ESI) represents the FESEM images of the perovskite NSs prepared at different T_s. Prior to the solvothermal treatment, narrow and long NR with width ~210 nm and length ~8 μm is observed from the reaction at room temperature (RT), as shown in Figure S1(a) (ESI), while the inset shows a magnified view of the NR. At T_s = 60 °C (PB60), the width of NR is dynamically increased to ~2 μm due to the lateral self-assembly of thin NRs (Figure S1(b) (ESI)). Figure S1(c) (ESI) depicts the formation of thick NS for PB100 as a result of the lateral attachment of the NRs. At T_s = 150 °C, the thinner NS is formed in PB150, as shown in Figure S1(d) (ESI), due to hindrance in the vertical growth of the sheet in the presence of surface ligands. Note that the ultrathin NSs for PB150 cannot be fully discerned in the FESEM image due to its resolution limit. Figure S1(e) (ESI) is the FESEM image of PB60 on which the elemental mapping was performed. Figure S1(f-i) (ESI) depict the corresponding elemental mapping of Pb, Br, N, and C, respectively, showing the spatial distribution of each component. The images represent the uniform distribution of all the elements of $MAPbBr_3$ throughout the NRs and hence the formation of perovskite NS with a distinct shape is confirmed.

To understand the structural evolution of perovskite NS with the solvothermal treatment, TEM images were recorded at different stages of solvothermal growth. For the sample PB0, synthesized by simply mixing the precursors at RT without any special treatment, randomly oriented NRs are observed. At T_s = 60 °C (PB60), lateral self-assembly of NRs occurs in the

presence of an optimum concentration of capping ligand, as shown in Figure 1(a). The corresponding HRTEM lattice fringe pattern for PB60 with lattice spacing 0.32 nm is shown in Figure 1(b) and the inset shows the corresponding inverse fast Fourier transform (IFFT) image. Further increase in T_s to 100 °C results into the compact attachment of the self-assembled NRs to form large-area 2D nanosheet (NS), as revealed in Figure 1(c). Figure 1(d) depicts the HRTEM lattice fringe pattern of well crystalline perovskite NS in PB100. The calculated lattice spacing of 0.26 nm and 0.31 nm corresponds to the (210) and (200) planes, respectively, of the $MAPbBr_3$ crystals (see the inset of Figure 1(d)), suggesting the cubic structure corresponding to the space group Pm3m (221). For PB150, perovskite NS along with QDs is observed due to the increased Ts, as shown in Figure 1(e). Interestingly, the thickness of the NS is much reduced in PB150 as compared to that of PB100, which will be evident from the AFM analysis discussed later. Figure 1(f) demonstrates the HRTEM lattice fringe pattern of PB150, and the calculated lattice spacing is 0.27 nm corresponding to (210) plane. Finally, for PB180, the 2D NSs are disintegrated into 2D QDs, as shown in Figure 1(g), revealing the uniform distribution of QDs and the corresponding size distribution with an average size of 2.9 nm is shown in the inset. Figure 1(h) shows the HRTEM lattice fringe pattern a 2D QD, implying highly crystalline nature with a lattice spacing of 0.21 nm, which corresponds to (220) plane of $MAPbBr_3$. Since the size of the NCs is comparable/less than the exciton Bohr radius in bromide based perovskite (~ 4 nm), these are termed as QDs.

The current solvothermal method enables us to successfully tailor the morphology/thickness of the perovskite NSs from thick NRs to ultrathin 2D NS and finally to 2D QDs. The key factors in controlling the morphology are the solvothermal temperature, duration, and surfactant concentration. Inside the autoclave, the solvent cannot evaporate, and when the temperature and pressure of the solvent are increased above a critical point, the solvent becomes a supercritical fluid phase, which shows the characteristics of both the liquid

and gas phases and this supercritical fluid exhibits high viscosity and easily dissolve the chemical compounds that are insoluble under ambient conditions.[36] To optimize the growth and tune the perovskite NSs, the concentration of OAm and the time duration of solvothermal treatment were varied for PB100 sample (i.e., at T_s = 100 °C) keeping all other parameters unchanged (see Figure S2 (ESI)). Randomly oriented NRs along with small area thick NSs are observed at 30 µl OAm content, as shown in Figure S2(a) (ESI). For 200 µl OAm concentration, the NSs are fully disintegrated to QDs with very high blue emission under UV light, as revealed from Figure S2(b) (ESI) and its inset. Thus, it can be concluded that the OAm concentration has a strong impact on controlling the morphology of the perovskite NS. Next, by keeping the OAm concentration and T_s fixed at 60 µl and 100 °C, respectively, an extension of the solvothermal treatment duration from 30 min to 2h results into the formation of 2D NS decorated with QDs, as shown in Figure S2(c) (ESI). When the solution is solvothermally treated with a high concentration of surface ligand, more nuclei are formed, and its growth is dynamically controlled in all the directions, resulting in smaller nuclei.[14] Further, as the solvothermal reaction time is increased, keeping the temperature constant, the ligands get more time to react with the precursor nuclei and disintegrate the NSs resulting in the formation of NCs. Hence, OAm is key to control the kinetics of crystallization and controls the thickness of the nanostructure, while OA suppresses the NS aggregation and increases the colloidal stability[3]. Note that the synthesis process with only 1-octadecene resulted into the formation of non-uniform nanostructures, and tuning of the morphology and the optical band gap was not achievable with the variation of reaction time and temperature. In contrast, the combination of OAm and OA allowed us to tune the thickness, morphology and the optical properties of the NS systematically. Thus, at an optimum growth condition (60 µl OAm and 30 min solvothermal treatment), the self-assembly process of NRs and nanoplatelet have been observed to take place due to the destabilization of the surface ligands caused by the elevated

autoclave pressure and temperature. Without any pretreatment, the DMF solution slowly reacted with the capping ligands inside the autoclave and arranged in a specific direction. It has been reported that high pressure inside the closed chamber of the autoclave is a key factor in assembling the randomly oriented NRs in a specific direction.[30] At elevated pressure and temperature, controlled evaporation of the solvent in solvothermal method increase the viscosity of the growth medium which facilitates the lateral oriented attachment of the NRs and platelets to form NSs due to lack of free volume and spatial constraints.[37] Interestingly, we observe a dramatic change in the structural parameter in the perovskite crystal at T_s = 150 ºC (discussed later). At this temperature, the as-grown NSs consist of bilayer perovskite.

Note that pressure-induced phase transition and self-assembly of NR to from 2D NS have been reported earlier.[7, 18, 30, 37-39] The self-assembly of NRs can also be explained by considering the interaction energies between the NRs. According to the classical theory of interaction between nanoparticles, two dominating forces responsible for the self-assembly process of NSs are the van der Waals force, and electrostatic interaction. The repulsion forces arise from the net charges and the steric repulsion of organic ligands.[21] The electrostatic repulsion force between two interacting $MAPbBr_3$ NRs and nanoplatelet dominates at large separation, while the attractive van der Waals force dominates at a short distance, and for the self-assembly of two NRs, they have to overcome an energy barrier of ~$0.25k_BT$.[21] Hence, at room temperature, it is very difficult for the NSs to be self-organized in a particular direction. In the solvothermal method, high pressure and controlled temperature play crucial roles in supplying the required energy to the NRs, and they attach laterally to each other to form large-area NSs. At higher reaction temperature, due to the increased thermal energy liquid-phase exfoliation of layers occurs giving rise to the thinning of the 2D layers down to 1.2 nm (bilayer perovskite) at 150 ºC (discussed below).

In order to estimate the thickness of the 2D perovskite NS precisely, AFM images were recorded in the tapping mode. Figure 2(a) shows the AFM image and the corresponding height profile of PB0, revealing the thickness of the NR as ~67 nm. Figure 2(b) exhibits the AFM image of PB60, and the thickness of the NR is found to be ~18.5 nm. Figure 2(c) demonstrates the formation of thin NS in PB100 and the average thickness of the NS is found to be ~8.4 nm. The AFM images of thin NSs in PB120 and PB130 are shown in Figure 2(d,e) and the corresponding thicknesses are found to be ~6.3 nm and ~4.8 nm, respectively. Figure 2(f,g) depict the AFM images of PB140 and PB150 NS, respectively. Interestingly, the thicknesses of PB140 and PB150 NS are further reduced to ~3.2 nm and ~1.2 nm, respectively, as depicted in their respective height profiles. For PB180, a uniform distribution of QDs is observed as seen in the AFM image shown in Figure 2(h) and the corresponding thickness of the QDs is estimated to be ~1.2 nm. Considering the unit cell size of $MAPbBr_3$ as 5.93 Å, the number of unit cell layers (n) was estimated from the thickness of the NSs/QDs to be: n ≈ 14, 10, 8, 5, 2 and 2 for the samples grown at 100, 120, 130, 140, 150 and 180 °C, respectively.[15] Thus, we have successfully tuned the thickness of the NS precisely from 14 layers (14L) to 2L by systematically increasing the solvothermal reaction temperature. The thickness of the NS and QDs is comparable to or less than the 3D exciton Bohr radius of $MAPbBr_3$ (~ 4.4 nm); hence a strong QC effect can be expected in the optical properties of the NSs. It is reported that oleic acid is densely packed in an ordered layer on the NS surface, thus helps in stabilizing the 2D NS growth.[40] Here, tuning the thickness of 2D NS is achieved by the increased reactivity of OAm due to the high pressure and temperature inside the autoclave. At low temperature where the interplanar spacing is less, the surface ligands can't enter between the layers and exfoliation of layer can't occur. But, at high temperatures the interplanar spacing is enlarged (discussed from XRD analysis), and the surface ligands can successfully exfoliate the NS layer giving rise to thinner NS.[41] Hence, the surface ligands are attached to the surface of the NSs and selectively

exfoliate the layers of the NSs along the vertical direction, promoting thinner sheets at higher temperature. Thus, the control of growth and morphology of colloidal NSs are achieved by a kinetically controlled process, governed by the temperature-dependent dynamic surface −ligand interaction.

3.2. Structural and compositional analysis

Results of XRD measurements presented in Figure 3(a) exhibit that the initial cubic structure of the perovskite solution is retained in the course of the self-assembly process in solvothermal treatment. XRD patterns of $MAPbBr_3$ NSs indicate a pure cubic phase, perfectly assigned to Pm-3m space group (Figure 3(a)). Note that in the XRD pattern, (130) peak is dominant in PB180 and the intensity of (100) peak is lower than that of (110) peak in PB180 indicating ultrathin 2D QDs. The comparison of interplanar spacing corresponding to (100) diffraction peak for different growth temperatures is shown in Figure 3(b). It is worth noting that there is a systematic increase in lattice spacing (d-spacing) (from 5.82 Å at RT to 5.89 Å at 180 °C) with increasing temperature and reduction in sheet thickness. Note that with the increase in T_s the morphology of the NS is changed from thick NR to ultra-thin NS to ultrathin QDs and thus, the (100) diffraction peak position is observed to be shifted towards lower angle (~0.18 ° shift), indicating lattice expansion and marginal broadening in full width at half maxima (FWHM) (0.079 to 0.108 °). Since the NSs are highly anisotropic, the Scherrer equation cannot be employed to determine the dimension from the observed FWHM. Hence, the thickness of the NSs is measured directly from AFM height profile analysis. The right Y-axis of Figure 3(b) displays the comparison of (100) diffraction peak intensity with the increase in T_s, reaction temperature. Characteristic XRD peak intensity (100) systematically decreases with increasing T_s; especially at 150 °C the (100) peak intensity reduces largely indicating exfoliation of the sheets perpendicular to (100) direction leading to bilayer perovskite (thickness, ~1.2 nm). The (100) oriented 2D perovskite can be categorized as Ruddlesden-

Popper phase.[42] Figure 3(c) shows the variation in NS thickness with T_s. This shows a systematic decrease in thickness (d) linearly (as shown by the linear fit) with increasing temperature (T). The negative coefficient of the temperature term indicates dissociation energy, which is obviously proportional to T. We believe that as the d-spacing increases with increasing temperature, more of OAm enters in between the two layers of perovskite NS and results into exfoliation/separation of layers to thinner layers down to 1.2 nm thin 2D layer. A schematic of the possible growth mechanism and shape evolution from randomly oriented NR to 2D QDs is presented in Figure 3(d). It is interesting to note the systematic decrease in intensity of (100) peak in XRD pattern with increasing T_s due to the thinner layers cleaved from the cleavage (100) plane. The XRD patterns of pure $MAPbX_3$ (X= I, Br and Cl) and mix halide perovskite NSs synthesized at 100 °C are shown in Figure S3(a,b) (ESI). When the halide composition is changed from iodide to bromide and towards chloride, the characteristic XRD peaks systematically shift towards higher diffraction angles (see Figure S3(b), ESI), which can be attributed to the decrease in radii of halide ions from iodide to bromide and chloride.[14]

The chemical valence state, composition, and surface properties of PB100 and PB150 NSs were investigated using the XPS analysis. The XPS spectrum of Br 3d is presented in Figure 4(a), which is deconvoluted with two peaks centered at 68.9 ($3d_{5/2}$) and 70.6 eV ($3d_{3/2}$), corresponding to the inner and surface Br ions, respectively. In Figure 4(b), the XPS spectrum of Br 3d corresponding to PB150 NS is presented with Gaussian deconvoluted peaks centered at 68.6 and 70.0 eV. Hence, there is a marginal shift (~0.3 eV and ~0.6 eV) in binding energy (BE) in thinner PB150 NS corresponding to Br $3d_{5/2}$ and Br $3d_{3/2}$ respectively, revealing good surface properties even for higher reaction temperature. Note that the intensity ratio of Br $3d_{3/2}$ peak to $3d_{5/2}$ peak is marginally higher for PB150 (~0.38) than that in PB100 (~0.21) suggesting a Br rich surface in case of thinner NSs. This is consistent with the decrease in the thickness of the NS in PB150 as compared to PB100. In Figure 4(c,d), the XPS spectrum of Pb^{2+} (Pb 4f)

for PB100 and PB150 exhibit two symmetric peaks, which are attributed to Pb $4f_{7/2}$ and Pb $4f_{5/2}$ levels at BE of 138.7 eV and 143.6 eV, respectively. The spin-orbit split between the Pb $4f_{7/2}$ and Pb $4f_{5/2}$ levels for both the NSs was found to be 4.9 eV, which matches well with the reported value (4.8 eV).[2] In our system, the contribution of metallic Pb at a lower binding energy (136.8 eV) is not observed, indicating no partial reduction/oxidation of Pb.

3.3. Optical analysis

3.3.1. UV-Vis absorption and photoluminescence studies

UV-Vis absorption and PL emission spectra of various perovskite NSs are shown in Figure 5(a) and the inset shows the corresponding photographs of the $MAPbBr_3$ NS suspensions in toluene excited by UV light. The PL emission spectra were recorded with 400 nm excitation. The apparent emission color of the solutions systematically changed from green (PB0) via blue-green (PB150) to cyan (PB180). Correspondingly, there is a systematic blue shift of the absorption edge and PL peak (from 530.0 nm in PB0 to 488.2 nm in PB180) in the respective spectrum with the increase in reaction temperature. The systematic blue shift can be attributed to the systematic reduction in the thickness of the NS down to 1.2 nm. PL spectrum for PB180 QDs possesses relatively broader PL linewidth (41.6 nm) as compared to that of 2D NS in PB150 (22.8 nm), which may be associated with the size distribution of the perovskite QDs. Note that PL peak energy is successfully tuned by ~200 meV (~42 nm) by tailoring the thickness of the NSs. The tailoring of PL emission peak from green (530.0 nm) to cyan (488.2 nm) region may be caused by the strong QC effect due to the reduced thickness of the 2D NS down to 2 layers and its final disintegration to 2D QDs. Note that PB150 and PB180 show excitonic features in the absorption spectra due to the transition to higher excited states (see Figure S4(a) (ESI)). The excitonic peaks shift towards higher energy region (~10 nm) for QDs in PB180 compared to NS in PB150 due to an increase in the bandgap. Further tuning of the PL emission to the blue region is achieved by changing the OAm concentration while

keeping the reaction temperature fixed at 100 °C. As the OAm amount is increased from 60 µl to 200 µl, the PL peak position is tuned from 518 nm to 458 nm, i.e., a large blue shift of 60 nm is observed (see Figure S4(b), ESI). Increase in the OAm concentration results into the formation of 2D QDs (discussed earlier), which in turn results into the shift in PL peak position to blue region due to strong confinement effect. Hence, using the solvothermal method, we could successfully synthesize the bright blue-emitting perovskite QDs. Similarly, by increasing the reaction duration to 2 hrs, the PL peak of PB100 NS is blue-shifted by ~28 nm (see Figure S4(c), (ESI)). The variation in PL intensity with the excitation wavelength is shown in Figure S4(d) (ESI) revealing the highest intensity of PL emission for 466 nm and 400 nm excitation for PB100 and PB140, respectively. However, PL peak position (energy) does not change with excitation wavelength. PL excitation spectra of PB100 with emission fixed at 518 nm and PB140 with emission fixed at 508 nm are shown in Figure S4(e,f) (ESI) along with absorbance data and it is clear that excitation spectrum is consistent with the absorption spectrum in each sample. The presence of additional peaks in the PL excitation spectrum besides the sharp absorption edge suggests the possible involvement of additional sates in the PL emission spectra, which is discussed later.

The tunable optical properties of the NS can be explained by considering the perovskite crystal structure. The ultrathin NS is comprised of layers of corner-sharing $PbBr_6$ octahedra, with the capping ligand around the NS, leading to the confinement of electrons giving rise to discrete energy levels.[10] Exciton Bohr radius of bromide perovskite is reported to be ~4.4 nm, which is higher than the thickness of NS in PB140 (5 layers). Hence, we consider the perovskite NS in PB140, PB150, and PB180 to be in the strong confinement regime resulting in cyan emitting NS and QDs under UV light. Note that the increase in the bandgap in perovskite has also been associated with the lattice contraction/distortion. However, we observed a systematic expansion of the lattice with increasing reaction temperature i.e. with reduced thickness (see

Figure 3(b)). In general, lattice expansion is expected to give rise to a red shift of the bandgap. However, a systematic blue shift in the absorption edge and PL peak is observed in our case, which is contrary to the behavior expected from lattice expansion. This confirms the fact that the systematic blue shift in the absorption edge is not related to change in the lattice constant, but it is due to the ultra-small thickness of the layers that gives rise to the QC effect. To assess the QC effect qualitatively, we have plotted the optical bandgap vs NS thickness in Figure 5(b). The optical band gap was calculated from the absorption spectra of different samples. Interestingly, thickness dependence of the optical bandgap data follows the Brus model of QC using the effective mass approximation (EMA)[43]:

$$E_g = E_0 + h^2/8\mu_{ef}d^2 - 1.786e^2/4\pi\varepsilon_0\varepsilon_r d \quad (1)$$

Where E_0 is the bulk bandgap, d is the 2D layer thickness, h is the Planck's constant, μ_{ef} is the effective exciton reduced mass, and ε_r is the dielectric constant. From the fitting of E_g vs. d plot, the extracted parameters are: μ_{ef} = 0.114m_0, ε_r = 9.8, which match well with earlier reports[44-45]. Here m_0 is the free electron mass. Taking the above values, the Bohr radius (R_B) of $MAPbBr_3$ is calculated using the relation,

$$R_B = m_0\varepsilon_r R_H/\mu_{ef} \quad (2)$$

Where, R_H is Bohr radius of a hydrogen atom (0.053 nm). Exciton Bohr radius of $MAPbBr_3$ is found to be 4.6 nm, which closely matches with the reported values[45-46]. Hence, the change in the optical bandgap of the 2D perovskite layers with the 2D layer thickness clearly follows the QC model and thus the 2D NS can act as ideal platform for exploiting quantum effects in perovskite materials.

Interestingly, this simple solvothermal synthesis technique can be easily extended to fabricate colloidal PB100 NSs through halide substitutions. A series of colloidal $MAPbX_3$ NSs with tunable compositions were fabricated by the solvothermal treatment at 100 ºC using different combinations of PbX_2 salts, as shown in Figure 5(c), and the inset shows the evolution

of emission color under UV light excitation upon forming mixed-halide NSs (X = Br, Cl, and I). The absorption and PL spectra are finely tuned over the full visible range (450 to 656 nm) by varying the composition of cations. Band structure of halide perovskite is greatly influenced by the p-orbitals of lead and halogen (X = Cl, Br or I) atoms. Thus, a change in the halide composition of the perovskite from Cl to Br to I results into the change in the valence orbital of halide from 3p to 4p to 5p, respectively, causing a systematic reduction in the bandgap.[47] This can be clearly observed from the change in absorption edge from 443 nm for $MAPbCl_3$ to 514 nm for $MAPbBr_3$ to 643 nm for $MAPbI_3$. The systematic increase in optical bandgap from 1.8 eV to ~2.8 eV with halide exchange from I to Cl is exhibited in Figure 5(d). Hence, the band structure of halide perovskite is successfully tuned by our solvothermal method using a different combination of halide salts.

Importantly, the absolute PL QYs of the perovskite NSs are measured to be high and these tabulated in Table 1. The highest PL QY (78%) was achieved for the NS grown at T_s = 100 ºC. However, a further increase in T_s leads to thinning of the layers, and it affects the non-radiative/ radiative transition channels of photons indirectly, which in turn results in the reduction of the PL QYs of the NSs.[48] A closer look at the PL spectral features, including its asymmetry, reveals that each peak contains three emission peaks. Deconvulated PL spectra of PB100 NS with three peaks is shown in Figure 6(a). As the position of peak 1 closely matches with the QDs emission peak (see Figure 5(a)), the peak 1 is believed to originate from the 2D perovskite QDs that are simultaneously present along with the 2D NS surface. Peak 2, which is dominant and coincides with the absorption edge peaks is originated from NS band to band or band-edge emission[49]. Peak 3 is believed to be defect-related emission, including surface defect which is more dominant in thinner NS, such as PB150. The summary of the PL features are summarized with a band diagram showing the respective transitions in the inset of Figure 6(a). The deconvulated PL peaks of other samples are shown in Figure S5 (ESI). The details of the fitting parameters

of all samples are given in Table S1 (ESI). It is clear that the contribution of additional two peaks (1, 3) is significant for thinner NS such as PB150 as compared to that of PB100. It is quite expected, as with the decrease in the thickness of the NS, the presence of surface related defects and presence of QDs are prominent. From XPS analysis, it is inferred that PB 150 NS has more surface Br than PB100, which results into more surface defects in thinner NS. Note that PB100 shows much higher PL QY than that of PB150. As the reaction temperature is increased, the contribution of band edge emission decreased (see Table S1 (ESI)) and the contribution of defect-related emissions is increased, due to lower thickness of NS. This in turn results in the overall decrease in PL QY in thinner NS. Post-growth processing may be required to eliminate the influence of surface defects in the 2D NS for improving the overall PL QY.

3.3.2. Low-temperature photoluminescence studies

The temperature-dependent PL spectra of PB100 NS were investigated in the range of 80-300 K to study the origin of high PL QY and the excitonic properties. Figure 6(b) shows the temperature-dependent PL spectra of PB100 NS, revealing the systematic increase in PL intensity with decreasing temperature. The inset of Figure 6(b) shows the dependence of integrated PL intensity on temperature. Figure 6(c) shows the temperature-dependent integrated PL intensity, and the experimental data are fitted using the Arrhenius equation, given by,

$$I(T) = I_0/\left(1 + Aexp(-E_B/k_BT)\right), \quad (3)$$

where, $I(T)$ and I_0 are the integrated PL intensities at temperatures T and 0 K, respectively. A is a constant, and E_B is the exciton binding energy. To estimate the exciton binding energy of NS, the experimental data are fitted in the higher temperature region (160-300 K). From the fitting, E_B is found to be ~225±21 meV for PB100. Thus, the exciton binding energy in our 2D NS is ~4 times higher than that of its 3D bulk counterpart (30-76 meV) and it is consistent with our

previous report on perovskite QDs.[50] It also matches well with the theoretical limit[51]: $E_B^{2D} = 4 \times E_B^{3D}$. In 2D NS, due to its ultralow thickness, the Coulomb interaction between electron and hole is less screened, which in turn increases the exciton binding energy.[51] Though the exciton binding energy of bulk perovskite is large enough to show the excitonic effect at room temperature, the recombination is mainly dominated by the recombination of free electrons and holes, which may have resulted into the overestimation of exciton binding energy based on low-temperature experiments.[52] Hence the exciton binding energy extracted from the fitted data in high-temperature regime may be taken as an actual one, which is ~7 fold higher than the bulk one. This confirms that the PL emission in NS is from the exciton recombination due to enhanced exciton stability.[52] High exciton binding energy in PB100 NS supports the stable and high PL QY. The variation in PL peak energy with temperature is shown in Figure S6 (ESI), revealing ~45.8 meV upshift in PL peak with the increase in temperature. In perovskite semiconductor, the increase in bandgap with temperature is attributed to the electron-phonon coupling.[53] The exciton–phonon coupling leads to the shrinkage in band gap, which induces the red shift of the PL spectral peak with decreasing temperature. Hence, perovskite has a positive thermal expansion coefficient of the band gap. In order to estimate the electron-phonon coupling, the experimental data of PL peak position vs temperature is fitted with the equation,[50]

$$E_g(T) = E_0 + A_{TE}T + A_{EP}(1 + 2/(exp(\hbar\omega/k_BT) - 1)) \quad (4)$$

Where E_0 is the bandgap at 0 K, $\hbar\omega$ is the phonon energy, A_{TE} and A_{EP} are the factors accounting for thermal expansion and electron-phonon interaction, respectively. The parameters extracted from the fitting are: A_{TE}= 0.13 meV/K, A_{EP}= 17 meV, $\hbar\omega$= 37 meV, which match well with the literature.[4] Temperature-dependent linewidth ($\Gamma(T)$) of PL spectra is displayed in Figure 6(d). A broadening in PL peak at higher temperature is observed, which may be caused by the coupling of the excitons to acoustic phonons and to longitudinal optical (LO) phonons.[54] To

quantify the exciton-phonon interaction in the 2D NS, experimental data are fitted using Boson model given by:

$$\Gamma(T) = \Gamma_0 + \Gamma_{LO}/(exp(\hbar\omega_{LO}/K_B T) - 1) \quad (5)$$

Where Γ_0 is the inhomogeneous broadening contribution, Γ_{LO} is the longitudinal exciton-optical phonon contribution to the FWHM, and $\hbar\omega_{LO}$ is the LO phonon energy. The values of the fitted parameters are: Γ_0 = 33 meV, Γ_{LO} = 240 meV, $\hbar\omega_{LO}$= 36 meV, which are consistent with the unresolved vibration energy in the Raman spectrum.[55] Interestingly, the optical phonon energy extracted from Boson fit matches very well with that obtained from fitted data using equation (4). High optical phonon energy indicates strong exciton-phonon interactions, which is expected in a quantum confined system.

3.3.3. Time-resolved photoluminescence studies

Time-resolved photoluminescence (TRPL) measurement was performed on various perovskite NSs using a 405 nm pulsed laser excitation. The PL decay curves shown in Figure 7(a) are fitted with triexponential decay function given by $I(t) = \sum_{i=1}^{3} A_i \exp\left(-t/\tau_i\right)$ where A_i is the amplitude of the PL decay component corresponding to the lifetime τ_i. The average lifetime (τ_{avg}) is calculated using the relation: $\tau_{avg} = \sum_{i=1}^{3} A_i\tau_i^2 \Big/ \sum_{i=1}^{3} A_i\tau_i$. Based on the deconvolution of steady state PL spectrum with three peaks, the PL decay is fitted with triexponential decay function. The corresponding fitting parameters (see Table S1, ESI) including the evolution of the amplitude of each peak with solvothermal temperature is consistent with the steady state PL results. The contributions from three different states of different origin essentially suggest different time constants of each component. Slow component with high amplitude of the TRPL decay corresponds to the main PL contribution, i.e., band edge emission, while the faster lifetime component corresponds to the presence of QDs along with NS and defect states. As

shown in Table S1 (ESI), the average lifetime changes from 601.3 ns in PB0 to 67.0 ns PB180. Hence, a 9-fold decrease in PL lifetime is observed for the QDs due to the reduction in thickness/size. The variation in PL lifetime with the thickness of the 2D NS is presented in the inset of Figure 7(a), demonstrating a longer lifetime of carriers for the thicker NS grown at lower temperature suggesting a reduction in nonradiative recombination paths, which in turn yields high PL QY, suitable for optoelectronic device applications.[56]

3.3.4 Stability of the 2D NS

Stability of 2D NS is studied under different conditions. In order to evaluate the stability of the NS under prolonged laser irradiation, we have recorded the PL spectra of PB140 NS at room temperature at a regular interval under continuous laser irradiation (405 nm, 15 mW at source). The variation of PL emission intensity with time under continuous laser irradiation for 7 hours in the ambient condition is shown in Figure 7(b). We observe first a gradual increase in PL intensity with laser exposure up to 2.5 hours of the laser irradiation of PB140 and then it marginally decreased followed by constant intensity, which is higher than its initial intensity. It is likely that due to local heating caused by the laser exposure, the structural and optical properties of the NS improved resulting in higher PL intensity after prolonged laser exposure. However, prolonged exposure leads to more stable performance of the NS. Hence, the 2D NS exhibits excellent optical stability under long hour laser irradiation. Effect of laser irradiation on the PL intensity is better understood by deconvolution of PL spectra for PB140 NS sample with three Gaussian peaks before and after laser irradiation for 3 hrs (see Figure S7(a,b), ESI). These three peaks are attributed to the presence of QDs, NS band-edge emission and defect-related emissions, as discussed earlier in detail. Before laser irradiation, the contribution of defect emission is prominent. However, after laser irradiation, the contribution of band edge emission peak is substantially increased as compared to that of defect, which in turn results into the higher intensity of emission. Tiguntseva et al. reported 130 % improved PL emission

in $CH_3NH_3PbI_3$ by laser post processing.[57] Gentle laser heating is reported to reduce the defect concentration in the perovskite film.[57] Tian et al. reported thousand fold enhancement in PL intensity and proposed that the trapping sites, which are responsible for non-radiative charge recombination, can be de-activated in the course of light curing process.[58] Mosoconi et al. reported the increase in PL lifetime and total intensity which eventually stabilize, due to reduction of an initial trap density of $\sim 10^{17}$ cm^{-3} to a stabilized trap density of $\sim 10^{16}$ cm^{-3}.[59] Thus, our results are consistent with the literature. Long-term storage stability of 2D NS in PB140 is also tested in the ambient environment. The sample was stored in an ambient condition with high humidity without any protection. Inset of Figure 7(b) exhibits the PL spectra of PB140 taken for a freshly prepared sample and that of after 8 months of storage. The PL intensity of PB140 is observed to be marginally reduced after 8 months of storage, indicating its high stability. Thus the NS retains its initial PL emission even after the storage for several months in high humidity ambient, which is the most unique property of 2D Ruddelson proper perovskite compared to its 3D counter part due to high formation energy, hydrophobic organic cations, strong Van-der Waals interaction between the capping organic molecules and the $[PbI_6]$ units.[60-61] However, PL intensity of PB150 NS decreases by >90% after storing it in ambient condition as shown in Figure S8(a) (ESI). NS in PB150 is of bilayer thickness, hence it may disintegrates to QDs in ambient condition as QD peak is prominent after 8 months. Further optimization of the process parameters may be required to increase the stability of bilayer NS.

Temperature dependent stability of PB140 NS is investigated by heating the sample at different temperatures and recording its PL spectra at each temperature. There is a systematic decrease in PL intensity with increasing temperature of heating (see Figure 7(c)), which is consistent with the thermal quenching behaviour of PL. To assess its structural stability after heating, XRD pattern was recorded before and after heating the sample at 80 ºC for 2 hours.

The XRD pattern intensity is increased after heating, as shown in the inset of Figure 7(c), and it implies the improved crystal structure of the NS after heating. Hence, the synthesized NS shows excellent structural and optical stability at higher temperature up to 80 ºC.

3.4. Performance of 2D perovskite NS as white LED

Practical application of the as-grown 2D NS is demonstrated by fabricating a white LED using a blue LED chip and $MAPbBr_1I_2$ layer. Mixed halide perovskite solution having emission at ~600 nm is first mixed with polymer and then it was used as an orange emissive layer on top of blue LED to fabricate the white LED. The electroluminescence spectra of the optimized white LED driven by bias voltage 2.35 V is shown in Figure 7(d) with upper inset showing the digital photograph of the device. The CIE coordinates of the device are found to be (0.33,0.30) with CCT 5263 and CRI 55 (see lower inset of Figure 7(d)). The CIE coordinates of the fabricated white LED is closely matches with the pure white light (0.33, 0.33). The performance and color purity of the orange luminescent perovskite coated white LED are comparable or better than other reported orange luminescent phosphor coated white LEDs using carbon dots, silicon dots and other 2D materials.[62-66] Hence, mixed halide perovskite can be considered as a promising candidate for the high color quality, low cost white light production and in the solid-state lighting field. Operational stability of fabricated LED is measured up to 7 h of continuous operation at 2.35V. It is observed that the intensity of blue emission from LED chip (encapsulated) is nearly unchanged, while the intensity of yellow emission from MAPbBr1I2 is decreased by about 20%, as shown in Figure S8(b) (ESI). Hence, white LED shows reasonably good stability without any encapsulation or protection. It is expected that encapsulation as well as device fabrication inside a glove box will improve the stability of the device much better.

3.5. Performance of 2D perovskite NS based photodetector

The 2D perovskite NSs with high lateral size (surface area) and long diffusion length are reported to be promising for various photovoltaic and optoelectronic applications[7, 9, 67]. Accordingly, a photodetector device was fabricated based on PB140 NSs in order to demonstrate its potential application. The schematic representation of the planar device structure and the energy band diagram are portrayed in Figure 8(a). Aluminum electrodes with an interdigital spacing of 100 μm were first deposited on the Si/SiO_2 substrate by thermal evaporation through a shadow mask. Subsequently, the NS solution was drop cast between the gap of two electrodes and dried at 60 °C. In the dark, very low current (dark current, I_{dark}) flows between two electrodes under an applied bias voltage. When the device was exposed to light (405 nm laser), it results in the generation of electron-hole pairs with an energy higher than the bandgap of the perovskite NS. The electron and holes are then rapidly drifted in different directions under bias voltage and collected by the electrodes leading to a dramatic increase in current (photocurrent, I_{ph}) between the metal electrodes. Figure 8(b) shows the I-V characteristics of the device obtained in the dark and under different intensities of light illumination (405 nm). Under the dark condition, nearly linear current-voltage (*I–V*) behavior is observed. Under illumination, the current is abruptly increased, implying good sensitivity of the device to light. The photocurrent is highly dependent on the light intensity, and it is systematically increased with the increase in the light intensity because the number of photogenerated carriers is proportional to the absorbed photon flux. The inset of Figure 8(b) shows the magnified view of I-V characteristic in the low bias region, indicating the turn-on voltage of the device is very low (~0.4 V). Figure 8(c) demonstrates the dependence of the photocurrent on light intensities under 2 V bias. This dependence can be understood better by fitting the data of photocurrent vs intensity by the well-known power law: $I_{Ph} \alpha P^{\theta}$, where I_{ph} is the photocurrent, P is the light intensity and θ is an empirical value reflecting the recombination of photocarriers, as shown in Figure 8(c).[68] In the low-intensity range, exponent θ=0.97 was

obtained, which is close to 1.0, suggesting a low recombination loss. In contrast, in high-intensity range, non-unity $\theta=0.12$ was observed, implying a strong recombination loss due to the presence of high carrier density and some trap states in the bandgap region.[69]

Typical temporal dependence of the photoresponse under pulsed laser illumination under different bias voltages is shown in Figure 8(d). The photoresponse of the device is observed to be highly stable and reproducible over the long operational duration as well as ambient storage. The rise and fall edges of the photoresponse curve are very steep, indicating the very fast response of the device.[68] The photocurrent increases linearly with increasing the bias voltage due to the efficient transport of photocarriers and the suppression of the recombination loss at higher bias voltage. At lower bias voltages region (0 to 1.5 V), the photocurrent increases very rapidly following a nonlinear behavior, as shown in the inset of Figure 8(d). To calculate the fast response speed of the device, temporal response curve was recorded in a digital oscilloscope at a bias voltage of 5 V using the 405 nm pulsed laser driven by a TTL pulse, as shown in Figure 9(a). Since the direct measurement of the photocurrent is inherently slow in an ammeter, a 100 kΩ load resistance is added in series to the circuit, and the voltage across the load is measured in the oscilloscope. The rise/fall time of the device is found to be very fast 24 μs/103 μs. Note that the photocurrent response of our photoconductor is much faster than those reported earlier on perovskite NS (see Table 2). This may be due to high crystalline quality and high mobility of the carriers in the as-grown 2D NS. Figure 9(b) presents the long term stability of the photodetector device. The temporal photoresponse curve of the freshly fabricated sample is presented in the first five cycles in Figure 9(b). The second and third five cycles in Figure 9(b) correspond to the temporal photoresponse curve recorded after 15 days and one month of storage, respectively, without any encapsulation. It is clear that a very marginal decay in photocurrent (~10.7 %) is observed after one month of storage, implying that the device retains its photodetection capability even under the ambient condition

with high humidity. Thus, it can be concluded that the as-synthesized perovskite NSs have very high ambient stability even under high humidity. Note that most of the reported perovskite photodetectors exhibit poor stability.[70-71] Figure 9(c) summarizes the evolution of the photocurrent under the continuous illumination of 405 nm laser light in ambient condition (relative humidity: 60–70%, temperature ~23 °C) without any encapsulation/protection for 7 h operation under bias voltage of 5 V. The photocurrent remains almost constant throughout the measurement period, indicating its outstanding repeatability and long term operational stability. To characterize the performance of the as-fabricated photodetector, responsivity, EQE and detectivity were calculated in the spectral range 310−800 nm. The efficiency of a photodetector is expressed in terms of spectral responsivity since it is directly proportional to the internal gain. Responsivity (*R*) of a photodetector can be defined as the photocurrent generated in the photodetector per unit power of the light incident on its effective area and can be expressed as,

$$R = \frac{I_{ph} - I_{dark}}{PA} \quad (6)$$

Here, *A* is the effective illuminated area (0.02 cm^2). As shown in Figure 9(c), the NS detector displays a good spectral selectivity with a reasonably flat response in the range 310-560 nm consistent with its absorption behavior. Interestingly, the present device shows high responsivity in the UV region and can be exploited as a UV photodetector. The detectivity (*D*) and external quantum efficiency (*EQE*) are also calculated using the following equations to express the figure of merits of the photodetector device,

$$D = R \times \left(\frac{A}{2qI_{dark}}\right)^{1/2} \quad (7)$$

$$EQE = R\frac{hc}{q\lambda} \quad (8)$$

Where *A* is the effective area of the photodetector in cm^2, *q* is the electronic charge, h is the Planck's constant, *c* is the light velocity in vacuum and λ is the wavelength of the incident light.

Hence, to achieve high detectivity of the device, high responsivity and low dark current are necessary. Figure S9(a) (ESI) shows the EQE of the device under 5 V bias. Figure S9(b) (ESI) depicts the detectivity in the spectral range of 310-800 nm under 5 V bias. Both the parameters demonstrate spectral trend similar to the responsivity data since they are proportional to responsivity. The peak detectivity and EQE of PB140 NS are observed to be 1.04×10^{12} Jones and 658 %, respectively. Note that the EQE of the device is very high (>100 %), which may be partly due to the tunneling of the carriers in the ultra-thin 2D NS. The 2D materials based UV-Visible photodetector is applicable in numerous fields, such as imaging sensing, optical communication, optical storage, electric arc detection in factories, etc.

4. Conclusion

In conclusion, a simple, reproducible and novel solvothermal synthesis route is developed here to successfully grow large-area 2D perovskite nanosheets with precisely tunable thickness and high optical quality and colloidal stability. Without any pretreatment of the precursors, simple solvothermal treatment at various temperatures (100-150 °C) allowed us to tailor the thickness of the large area (several micrometers) 2D NSs from 14 layers down to a bilayer thickness (1.2 nm), as revealed by systematic TEM and AFM analyses. The temperature-dependent thickness evolution is quantitatively analyzed based on the supplied thermal energy leading to the enlarged interlayer spacing and accelerated crystal growth along the lateral direction. Based on the tuning of the thickness of 2D NS, optical properties are precisely tuned with the growth temperature, which makes this method very attractive for various optoelectronic applications. The bandgap of the NS is effectively tuned from 2.34 eV to 2.54 eV owing to the strong quantum confinement effect in the 2D NS. 2D NSs (PB150) and 2D QDs (PB180) with bilayer thickness fall in the strong quantum confinement regime, resulting in cyan light emission under UV irradiation. We have also demonstrated bright blue-emitting QDs by increasing the OAm concentration with very high PL QY of 84 % and large

spectral blue shift of ~60 nm. Low-temperature PL analysis revealed high exciton binding energy for the 2D NSs (225 meV) as compared to its 3D counterpart supporting the stable PL emission at room temperature. Higher lifetime of carriers in 2D NS is attributed to the long diffusion length, which is ideal for the photovoltaic/photodetection applications. The NS exhibits excellent optical and long-term stability including high temperature (up to 80 ºC) stability keeping its initial PL intensity retained for more than 6 months. The photodetector device based on the PB140 NS exhibited very high responsivity and fast response time (~a few μs), as compared to the literature reports. Most importantly, the as-fabricated device is highly stable in a humid environment and the photodetection performance/stability can be further improved by incorporating transport layers and a proper encapsulation. Thus, we believe that the new route developed here to synthesize highly stable large-area 2D organometal halide perovskite NSs and highly emissive QDs can be utilized in various optoelectronic and printing applications.

Supporting Information

Electronic supporting information file contains figures on the schematic of the synthesis process, TEM, XRD, PL, and photodetector performance data.

Acknowledgments

We acknowledge the financial support from DEITY (Grant No. 5(9)/2012-NANO (VOL-II)) for carrying out part of this work. Central Instruments Facility, I.I.T. Guwahati is acknowledged for providing the TEM and FESEM facilities. We thank Dr. H. Sugimoto, Kobe University, Japan, for help in the XPS measurement.

References

(1) Huang, H.; Zhao, F.; Liu, L.; Zhang, F.; Wu, X.-g.; Shi, L.; Zou, B.; Pei, Q.; Zhong, H. Emulsion Synthesis Of Size-Tunable CH3NH3PbBr3 Quantum Dots: An Alternative Route Toward Efficient Light-Emitting Diodes. *ACS Appl. Mater. Interfaces* **2015,** *7* (51), 28128-28133.
(2) Gonzalez-Carrero, S.; Galian, R. E.; Pérez-Prieto, J. Maximizing the Emissive Properties of CH3NH3PbBr3 Perovskite Nanoparticles. *J. Mater. Chem. A* **2015,** *3* (17), 9187-9193.
(3) Zhang, F.; Zhong, H.; Chen, C.; Wu, X.-g.; Hu, X.; Huang, H.; Han, J.; Zou, B.; Dong, Y. Brightly Luminescent and Color-Tunable Colloidal CH3NH3PbX3 (X= Br, I, Cl) Quantum Dots: Potential Alternatives for Display Technology. *ACS nano* **2015,** *9* (4), 4533-4542.
(4) Zheng, K.; Zhu, Q.; Abdellah, M.; Messing, M. E.; Zhang, W.; Generalov, A.; Niu, Y.; Ribaud, L.; Canton, S. E.; Pullerits, T. n. Exciton Binding Energy and the Nature of Emissive States in Organometal Halide Perovskites. *J. Phys. Chem. Lett.* **2015,** *6* (15), 2969-2975.
(5) Chen, F.; Xu, C.; Xu, Q.; Zhu, Y.; Qin, F.; Zhang, W.; Zhu, Z.; Liu, W.; Shi, Z. Self-Assembled Growth of Ultrastable CH3NH3PbBr3 Perovskite Milliwires for Photodetectors. *ACS Appl. Mater. Interfaces* **2018,** *10* (30), 25763-25769.
(6) Kumar, P.; Muthu, C.; Nair, V. C.; Narayan, K. S. Quantum Confinement Effects in Organic Lead Tribromide Perovskite Nanoparticles. *J. Phys. Chem. C* **2016,** *120* (32), 18333-18339.
(7) Liu, J.; Song, K.; Shin, Y.; Liu, X.; Chen, J.; Yao, K. X.; Pan, J.; Yang, C.; Yin, J.; Xu, L.-J.; Yang, H.; El-Zohry, A. M.; Xin, B.; Mitra, S.; Hedhili, M. N.; Roqan, I. S.; Mohammed, O. F.; Han, Y.; Bakr, O. M. Light-Induced Self-Assembly of Cubic CsPbBr3 Perovskite Nanocrystals into Nanowires. *Chem. Mater.* **2019**.
(8) Xing, J.; Liu, X. F.; Zhang, Q.; Ha, S. T.; Yuan, Y. W.; Shen, C.; Sum, T. C.; Xiong, Q. Vapor Phase Synthesis of Organometal Halide Perovskite Nanowires for Tunable Room-Temperature Nanolasers. *Nano Lett.* **2015,** *15* (7), 4571-4577.
(9) Ha, S. T.; Liu, X.; Zhang, Q.; Giovanni, D.; Sum, T. C.; Xiong, Q. Synthesis of Organic–Inorganic Lead Halide Perovskite Nanoplatelets: Towards High-Performance Perovskite Solar Cells and Optoelectronic Devices. *Adv. Opt. Mater* **2014,** *2* (9), 838-844.
(10) Sichert, J. A.; Tong, Y.; Mutz, N.; Vollmer, M.; Fischer, S.; Milowska, K. Z.; García Cortadella, R.; Nickel, B.; Cardenas-Daw, C.; Stolarczyk, J. K. Quantum Size Effect in Organometal Halide Perovskite Nanoplatelets. *Nano Lett.* **2015,** *15* (10), 6521-6527.
(11) Tyagi, P.; Arveson, S. M.; Tisdale, W. A. Colloidal Organohalide Perovskite Nanoplatelets Exhibiting Quantum Confinement. *J. Phys. Chem. Lett.* **2015,** *6* (10), 1911-1916.
(12) Cho, J.; Choi, Y.-H.; O'Loughlin, T. E.; De Jesus, L.; Banerjee, S. Ligand-Mediated Modulation of Layer Thicknesses of Perovskite Methylammonium Lead Bromide Nanoplatelets. *Chem. Mater.* **2016,** *28* (19), 6909-6916.
(13) Song, J.; Xu, L.; Li, J.; Xue, J.; Dong, Y.; Li, X.; Zeng, H. Monolayer and Few-Layer All-Inorganic Perovskites as a New Family of Two-Dimensional Semiconductors for Printable Optoelectronic Devices. *Adv. Mater* **2016,** *28* (24), 4861-4869.
(14) Chen, M.; Zou, Y.; Wu, L.; Pan, Q.; Yang, D.; Hu, H.; Tan, Y.; Zhong, Q.; Xu, Y.; Liu, H.; Sun, B.; Zhang, Q. Solvothermal Synthesis of High-Quality All-Inorganic Cesium Lead Halide Perovskite Nanocrystals: from Nanocube to Ultrathin Nanowire. *Adv. Funct. Mater.* **2017,** *27* (23), 1701121.
(15) Levchuk, I.; Herre, P.; Brandl, M.; Osvet, A.; Hock, R.; Peukert, W.; Schweizer, P.; Spiecker, E.; Batentschuk, M.; Brabec, C. J. Ligand-Assisted Thickness Tailoring of Highly Luminescent Colloidal CH3NH3PbX3 (X = Br and I) Perovskite Nanoplatelets. *ChemComm* **2017,** *53* (1), 244-247.
(16) Shamsi, J.; Dang, Z.; Bianchini, P.; Canale, C.; Di Stasio, F.; Brescia, R.; Prato, M.; Manna, L. Colloidal Synthesis of Quantum Confined Single Crystal CsPbBr3 Nanosheets with Lateral Size Control up to the Micrometer Range. *J. Am. Chem. Soc.* **2016,** *138* (23), 7240-7243.
(17) Akkerman, Q. A.; Motti, S. G.; Srimath Kandada, A. R.; Mosconi, E.; D'Innocenzo, V.; Bertoni, G.; Marras, S.; Kamino, B. A.; Miranda, L.; De Angelis, F.; Petrozza, A.; Prato, M.; Manna, L. Solution Synthesis Approach to Colloidal Cesium Lead Halide Perovskite Nanoplatelets with Monolayer-Level Thickness Control. *J. Am. Chem. Soc.* **2016,** *138* (3), 1010-1016.

(18) Nagaoka, Y.; Hills-Kimball, K.; Tan, R.; Li, R.; Wang, Z.; Chen, O. Nanocube Superlattices of Cesium Lead Bromide Perovskites and Pressure-Induced Phase Transformations at Atomic and Mesoscale Levels. *Adv. Mater.* **2017,** *29* (18), 1606666.
(19) Subhani, W. S.; Wang, K.; Du, M.; Wang, X.; Yuan, N.; Ding, J.; Liu, S. Anti-Solvent Engineering for Efficient Semitransparent CH3NH3PbBr3 Perovskite Solar Cells for Greenhouse Applications. *J ENERGY CHEM* **2019,** *34*, 12-19.
(20) Luan, J.; Xu, J.; Chen, J.; Shi, X.; Zhang, B.; Dai, S.; Yao, J. Efficient Planar CH3NH3PbBr3 Perovskite Solar Cells Prepared at Room Temperature with Ionic-Liquids/Fullerene as an Electron Transport Bilayer. *J. Solid State Chem.* **2019,** *270*, 436-442.
(21) Wang, W.; Zhang, Y.; Wu, W.; Liu, X.; Ma, X.; Qian, G.; Fan, J. Quantitative Modeling of Self-Assembly Growth of Luminescent Colloidal CH3NH3PbBr3 Nanocrystals. *J. Phys. Chem. C* **2019,** *123* (20), 13110-13121.
(22) Yuan, Z.; Shu, Y.; Xin, Y.; Ma, B. Highly Luminescent Nanoscale Quasi-2d Layered Lead Bromide Perovskites with Tunable Emissions. *ChemComm* **2016,** *52* (20), 3887-3890.
(23) Gonzalez-Carrero, S.; Espallargas, G. M.; Galian, R. E.; Pérez-Prieto, J. Blue-Luminescent Organic Lead Bromide Perovskites: Highly Dispersible and Photostable Materials. *J. Mater. Chem. A* **2015,** *3* (26), 14039-14045.
(24) Dou, L.; Wong, A. B.; Yu, Y.; Lai, M.; Kornienko, N.; Eaton, S. W.; Fu, A.; Bischak, C. G.; Ma, J.; Ding, T.; Ginsberg, N. S.; Wang, L.-W.; Alivisatos, A. P.; Yang, P. Atomically Thin Two-Dimensional Organic-Inorganic Hybrid Perovskites. *Science* **2015,** *349* (6255), 1518.
(25) Zhang, D.; Zhou, W.; Liu, Q.; Xia, Z. CH3NH3PbBr3 Perovskite Nanocrystals Encapsulated in Lanthanide Metal–Organic Frameworks as a Photoluminescence Converter for Anti-Counterfeiting. *ACS Appl. Mater. Interfaces* **2018,** *10* (33), 27875-27884.
(26) Zhang, T.; Yang, M.; Benson, E. E.; Li, Z.; van de Lagemaat, J.; Luther, J. M.; Yan, Y.; Zhu, K.; Zhao, Y. A Facile Solvothermal Growth of Single Crystal Mixed Halide Perovskite CH3NH3Pb(Br1−xClx)3. *ChemComm* **2015,** *51* (37), 7820-7823.
(27) Zhai, W.; Lin, J.; Li, C.; Hu, S.; Huang, Y.; Yu, C.; Wen, Z.; Liu, Z.; Fang, Y.; Tang, C. Solvothermal Synthesis of Cesium Lead Halide Perovskite Nanowires with Ultra-High Aspect Ratios for High-Performance Photodetectors. *Nanoscale* **2018,** *10* (45), 21451-21458.
(28) Chen, M.; Hu, H.; Tan, Y.; Yao, N.; Zhong, Q.; Sun, B.; Cao, M.; Zhang, Q.; Yin, Y. Controlled Growth of Dodecapod-Branched CsPbBr3 Nanocrystals and Their Application in White Light Emitting Diodes. *NANO ENERGY* **2018,** *53*, 559-566.
(29) Xia, H.-R.; Sun, W.-T.; Peng, L.-M. Hydrothermal Synthesis of Organometal Halide Perovskites for Li-Ion Batteries. *ChemComm* **2015,** *51* (72), 13787-13790.
(30) Li, Z.-J.; Hofman, E.; Davis, A. H.; Maye, M. M.; Zheng, W. General Strategy for the Growth of CsPbX3 (X = Cl, Br, I) Perovskite Nanosheets from the Assembly of Nanorods. *Chem. Mater.* **2018,** *30* (11), 3854-3860.
(31) Zhai, W.; Lin, J.; Li, Q.; Zheng, K.; Huang, Y.; Yao, Y.; He, X.; Li, L.; Yu, C.; Liu, C.; Fang, Y.; Liu, Z.; Tang, C. Solvothermal Synthesis of Ultrathin Cesium Lead Halide Perovskite Nanoplatelets with Tunable Lateral Sizes and Their Reversible Transformation into Cs4PbBr6 Nanocrystals. *Chem. Mater.* **2018,** *30* (11), 3714-3721.
(32) Chen, L.-J.; Lee, C.-R.; Chuang, Y.-J.; Wu, Z.-H.; Chen, C. Synthesis and Optical Properties of Lead-Free Cesium Tin Halide Perovskite Quantum Rods with High-Performance Solar Cell Application. *J. Phys. Chem. Lett* **2016,** *7* (24), 5028-5035.
(33) Chen, D.; Chen, X.; Li, J.; Li, X.; Zhong, J. Ultrathin CsPbX3 (X = Cl, Br, I) Nanoplatelets: Solvothermal Synthesis and Optical Spectroscopic Properties. *Dalton Trans.* **2018,** *47* (29), 9845-9849.
(34) Chen, L.-J.; Dai, J.-H.; Lin, J.-D.; Mo, T.-S.; Lin, H.-P.; Yeh, H.-C.; Chuang, Y.-C.; Jiang, S.-A.; Lee, C.-R. Wavelength-Tunable and Highly Stable Perovskite-Quantum-Dot-Doped Lasers with Liquid Crystal Lasing Cavities. *ACS Appl. Mater. Interfaces* **2018,** *10* (39), 33307-33315.

(35) Gadea, G.; Morata, A.; Tarancon, A. Chapter Five - Semiconductor Nanowires for Thermoelectric Generation. In *SEMICONDUCT SEMIMET*; Mokkapati, S.; Jagadish, C., Eds.; Elsevier: 2018; pp 321-407.
(36) Zhong, H.; Mirkovic, T.; Scholes, G. D. 5.06 - Nanocrystal Synthesis. In *Comprehensive Nanoscience and Technology*; Andrews, D. L.; Scholes, G. D.; Wiederrecht, G. P., Eds.; Academic Press: Amsterdam, 2011; pp 153-201.
(37) Mallavajula, R. K.; Archer, L. A. Nanocrystal Self-Assembly Assisted by Oriented Attachment. *Angew. Chem. Int. Ed.* **2011,** *50* (3), 578-580.
(38) Schettino, V.; Bini, R. Constraining Molecules at the Closest Approach: Chemistry at High Pressure. *Chem. Soc. Rev.* **2007,** *36* (6), 869-880.
(39) Yin, T.; Fang, Y.; Chong, W. K.; Ming, K. T.; Jiang, S.; Li, X.; Kuo, J.-L.; Fang, J.; Sum, T. C.; White, T. J.; Yan, J.; Shen, Z. X. High-Pressure-Induced Comminution and Recrystallization of CH3NH3PbBr3 Nanocrystals as Large Thin Nanoplates. *Adv. Mater* **2018,** *30* (2), 1705017.
(40) Udayabhaskararao, T.; Kazes, M.; Houben, L.; Lin, H.; Oron, D. Nucleation, Growth, and Structural Transformations of Perovskite Nanocrystals. *Chem. Mater.* **2017,** *29* (3), 1302-1308.
(41) Jian, M.; Liu, H.; Williams, T.; Ma, J.; Wang, H.; Zhang, X. Temperature-Induced Oriented Growth of Large Area, Few-Layer 2d Metal–Organic Framework Nanosheets. *Chem. Commun.* **2017,** *53* (98), 13161-13164.
(42) Mao, L.; Stoumpos, C. C.; Kanatzidis, M. G. Two-Dimensional Hybrid Halide Perovskites: Principles and Promises. *J. Am. Chem. Soc.* **2019,** *141* (3), 1171-1190.
(43) Brus, L. Electronic Wave Functions in Semiconductor Clusters: Experiment and Theory. *J. Phys. Chem.* **1986,** *90* (12), 2555-2560.
(44) D'Innocenzo, V.; Grancini, G.; Alcocer, M. J. P.; Kandada, A. R. S.; Stranks, S. D.; Lee, M. M.; Lanzani, G.; Snaith, H. J.; Petrozza, A. Excitons Versus Free Charges in Organo-Lead Tri-Halide Perovskites. *Nat. Commun.* **2014,** *5*, 3586.
(45) Galkowski, K.; Mitioglu, A.; Miyata, A.; Plochocka, P.; Portugall, O.; Eperon, G. E.; Wang, J. T.-W.; Stergiopoulos, T.; Stranks, S. D.; Snaith, H. J.; Nicholas, R. J. Determination of the Exciton Binding Energy and Effective Masses for Methylammonium and Formamidinium Lead Tri-Halide Perovskite Semiconductors. *Energy Environ. Sci.* **2016,** *9* (3), 962-970.
(46) Wang, Q.; Liu, X.-D.; Qiu, Y.-H.; Chen, K.; Zhou, L.; Wang, Q.-Q. Quantum Confinement Effect and Exciton Binding Energy of Layered Perovskite Nanoplatelets. *AIP Adv.* **2018,** *8* (2), 025108.
(47) Roy, M.; Vikram; Banerjee, S.; Mitra, A.; Alam, A.; Aslam, M. Composition-Controlled Synthesis of Hybrid Perovskite Nanoparticles by Ionic Metathesis: Bandgap Engineering Studies from Experiments and Theoretical Calculations. *Chem. Eur. J.* **2019,** *25*, 9892.
(48) Xu, H.; Wang, J.; Xuan, T.; Lv, C.; Hou, J.; Zhang, L.; Dong, Y.; Shi, J. Convenient and Large-Scale Synthesis of High-Quality, All-Inorganic Lead Halide Perovskite Nanocrystals for White Light-Emitting Diodes. *CHEM ENG J* **2019,** *364*, 20-27.
(49) Ghosh, J.; Ghosh, R.; Giri, P. K. Strong Cathodoluminescence and Fast Photoresponse from Embedded CH3NH3PbBr3 Nanoparticles Exhibiting High Ambient Stability. *ACS Appl. Mater. Interfaces* **2019,** *11* (16), 14917-14931.
(50) Parveen, S.; Paul, K. K.; Das, R.; Giri, P. K. Large Exciton Binding Energy, High Photoluminescence Quantum Yield and Improved Photostability of Organo-Metal Halide Hybrid Perovskite Quantum Dots Grown on a Mesoporous Titanium Dioxide Template. *J. Colloid Interface Sci.* **2019,** *539*, 619-633.
(51) Shamsi, J.; Urban, A. S.; Imran, M.; De Trizio, L.; Manna, L. Metal Halide Perovskite Nanocrystals: Synthesis, Post-Synthesis Modifications, and Their Optical Properties. *Chem. Rev.* **2019,** *119* (5), 3296-3348.
(52) Tan, Z.-K.; Moghaddam, R. S.; Lai, M. L.; Docampo, P.; Higler, R.; Deschler, F.; Price, M.; Sadhanala, A.; Pazos, L. M.; Credgington, D.; Hanusch, F.; Bein, T.; Snaith, H. J.; Friend, R. H. Bright Light-Emitting Diodes Based on Organometal Halide Perovskite. *Nat Nanotechnol.* **2014,** *9*, 687.
(53) Li, J.; Yuan, X.; Jing, P.; Li, J.; Wei, M.; Hua, J.; Zhao, J.; Tian, L. Temperature-Dependent Photoluminescence Of Inorganic Perovskite Nanocrystal Films. *RSC Adv.* **2016,** *6* (82), 78311-78316.

(54) Franssen, G.; Litwin-Staszewska, E.; Piotrzkowski, R.; Suski, T.; Perlin, P. Optical and Electrical Properties of Homoepitaxially Grown Multiquantum Well InGaN/GaN Light-Emitting Diodes. *J. Appl. Phys.* **2003,** *94* (9), 6122-6128.
(55) Quarti, C.; Grancini, G.; Mosconi, E.; Bruno, P.; Ball, J. M.; Lee, M. M.; Snaith, H. J.; Petrozza, A.; De Angelis, F. The Raman Spectrum of the CH3NH3PbI3 Hybrid Perovskite: Interplay of Theory and Experiment. *J. Phys. Chem. Lett.* **2014,** *5* (2), 279-284.
(56) Tang, X.; Chen, W.; Liu, Z.; Du, J.; Yao, Z.; Huang, Y.; Chen, C.; Yang, Z.; Shi, T.; Hu, W.; Zang, Z.; Chen, Y.; Leng, Y. Ultrathin, Core–Shell Structured SiO2 Coated Mn2+-Doped Perovskite Quantum Dots for Bright White Light-Emitting Diodes. *Small* **2019,** *15* (19), 1900484.
(57) Tiguntseva, E. Y.; Saraeva, I. N.; Kudryashov, S. I.; Ushakova, E. V.; Komissarenko, F. E.; Ishteev, A. R.; Tsypkin, A. N.; Haroldson, R.; Milichko, V. A.; Zuev, D. A.; Makarov, S. V.; Zakhidov, A. A. Laser Post-Processing of Halide Perovskites for Enhanced Photoluminescence and Absorbance. *J. Phys.: Conf. Ser.* **2017,** *917*, 062002.
(58) Tian, Y.; Peter, M.; Unger, E.; Abdellah, M.; Zheng, K.; Pullerits, T.; Yartsev, A.; Sundström, V.; Scheblykin, I. G. Mechanistic Insights into Perovskite Photoluminescence Enhancement: Light Curing with Oxygen Can Boost Yield Thousandfold. *Phys. Chem. Chem. Phys.* **2015,** *17* (38), 24978-24987.
(59) Mosconi, E.; Meggiolaro, D.; Snaith, H. J.; Stranks, S. D.; De Angelis, F. Light-Induced Annihilation of Frenkel Defects in Organo-Lead Halide Perovskites. *Energy Environ. Sci.* **2016,** *9* (10), 3180-3187.
(60) Zheng, Y.; Niu, T.; Ran, X.; Qiu, J.; Li, B.; Xia, Y.; Chen, Y.; Huang, W. Unique Characteristics Of 2d Ruddlesden–Popper (2drp) Perovskite For Future Photovoltaic Application. *J. Mater. Chem. A* **2019,** *7* (23), 13860-13872.
(61) Zhang, L.; Liu, Y.; Yang, Z.; Liu, S. Two Dimensional Metal Halide Perovskites: Promising Candidates for Light-Emitting Diodes. *J ENERGY CHEM.* **2019,** *37*, 97-110.
(62) Li, X.; Liu, Y.; Song, X.; Wang, H.; Gu, H.; Zeng, H. Intercrossed Carbon Nanorings with Pure Surface States as Low-Cost and Environment-Friendly Phosphors for White-Light-Emitting Diodes. *Angew. Chem. Int. Ed.* **2015,** *54* (6), 1759-1764.
(63) Ren, J.; Sun, X.; Wang, Y.; Song, R.; Xie, Z.; Zhou, S.; Chen, P. Controllable Photoluminescent and Nonlinear Optical Properties of Polymerizable Carbon Dots and Their Arbitrary Copolymerized Gel Glasses. *Adv. Opt. Mater* **2018,** *6* (12), 1701273.
(64) Mandal, A. K.; Ray, M.; Rajapaksa, I.; Mukherjee, S.; Datta, A. Xylene-Capped Luminescent Silicon Nanocrystals: Evidence of Supramolecular Bonding. *J. Phys. Chem. C* **2012,** *116* (27), 14644-14649.
(65) Wang, Y.; Yin, Z.; Xie, Z.; Zhao, X.; Zhou, C.; Zhou, S.; Chen, P. Polysiloxane Functionalized Carbon Dots and Their Cross-Linked Flexible Silicone Rubbers for Color Conversion and Encapsulation of White LEDs. *ACS Appl. Mater. Interfaces* **2016,** *8* (15), 9961-9968.
(66) Huang, S. C.; Wu, J. K.; Hsu, W.-J.; Chang, H. H.; Hung, H. Y.; Lin, C. L.; Su, H.-Y.; Bagkar, N.; Ke, W.-C.; Kuo, H. T.; Liu, R.-S. Particle Size Effect on the Packaging Performance of YAG:Ce Phosphors in White LEDs. *Int. J. Appl. Ceram. Technol.* **2009,** *6* (4), 465-469.
(67) Xing, G.; Mathews, N.; Sun, S.; Lim, S. S.; Lam, Y. M.; Grätzel, M.; Mhaisalkar, S.; Sum, T. C. Long-Range Balanced Electron-and Hole-Transport Lengths in Organic-Inorganic CH3NH3PbI3. *Science* **2013,** *342* (6156), 344-347.
(68) Luo, L.-B.; Wu, G.-A.; Gao, Y.; Liang, L.; Xie, C.; Zhang, Z.-X.; Tong, X.-W.; Wang, T.; Liang, F.-X. A Highly Sensitive Perovskite/Organic Semiconductor Heterojunction Phototransistor and Its Device Optimization Utilizing the Selective Electron Trapping Effect. *Adv. Opt. Mater* **2019,** *7*, 1900272.
(69) Zhang, Z.-X.; Long-Hui, Z.; Tong, X.-W.; Gao, Y.; Xie, C.; Tsang, Y. H.; Luo, L.-B.; Wu, Y.-C. Ultrafast, Self-Driven, and Air-Stable Photodetectors Based on Multilayer PtSe2/Perovskite Heterojunctions. *J. Phys. Chem. Lett* **2018,** *9* (6), 1185-1194.
(70) Tian, W.; Zhou, H.; Li, L. Hybrid Organic–Inorganic Perovskite Photodetectors. *Small* **2017,** *13* (41), 1702107.
(71) Lu, H.; Tian, W.; Cao, F.; Ma, Y.; Gu, B.; Li, L. A Self-Powered and Stable All-Perovskite Photodetector–Solar Cell Nanosystem. *Adv. Funct. Mater.* **2016,** *26* (8), 1296-1302.

(72) Liu, X.; Yu, D.; Cao, F.; Li, X.; Ji, J.; Chen, J.; Song, X.; Zeng, H. Low-Voltage Photodetectors with High Responsivity Based on Solution-Processed Micrometer-Scale All-Inorganic Perovskite Nanoplatelets. *Small* **2017,** *13* (25), 1700364.
(73) Li, Y.; Shi, Z.; Lei, L.; Zhang, F.; Ma, Z.; Wu, D.; Xu, T.; Tian, Y.; Zhang, Y.; Du, G.; Shan, C.; Li, X. Highly Stable Perovskite Photodetector Based on Vapor-Processed Micrometer-Scale CsPbBr3 Microplatelets. *Chem. Mater.* **2018,** *30* (19), 6744-6755.

Table 1: Details of the NS samples with 2D layer thickness and their photoluminescence (PL) characteristics. For all the cases, the OAm amount 60 µl except for PB100/200 where it is 200 µl.

Sample code	Solvothermal temperature (°C)	Duration (min)	Thickness of 2D NS (nm)	PL peak position (nm)	PL QY (%)
PB60	60	30	18.5	525	64
PB100	100		8.4	518	78
PB120	120		6.4	515	59
PB130	130		4.8	512	43
PB140	140		3.2	508	38
PB150	150		1.2	499	32
PB180	180		1.2	488	30
PB100/200	100		-	458	84

Table 2: Comparison of the performance and stability of the perovskite 2D NS based photodetectors reported in the literature with the present work.

Active material	Measurement condition (voltage, wavelength)	Rise time/ Fall time (ms)	R (A/W)	Stability (days of storage)	Ref
$MAPbBr_3$ QDs	2 V, 405 nm	320, 280	0.223	20 (30% decrease in I_{ph})	[49]
$MAPbBr_3$ milliwire	2 V, 532 nm	407, 895	0.525	225*	[5]
$CsPbBr_3$ nanoplatelet	1.5 V, 442 nm	0.6, 0.9	34	47 (34% decrease in R)	[72]
$CsPbCl_3$ NS	8 V, 405 nm	70, 45	-	2	[27]
$CsPbBr_3$ microplatelet	5 V, 405 nm	20.9, 24.6	1.33	210 (10% decrease in I_{ph})	[73]
$MAPbBr_3$ NS	5 V, 405 nm	0.024, 0.103	1.93	180 (15% decrease[#] in PL)	*This work*

*I_{ph}=photocurrent, R=responsivity, * ~30% decrease in PL intensity after 140 min in 75% humidity, [#]under 70% humidity*

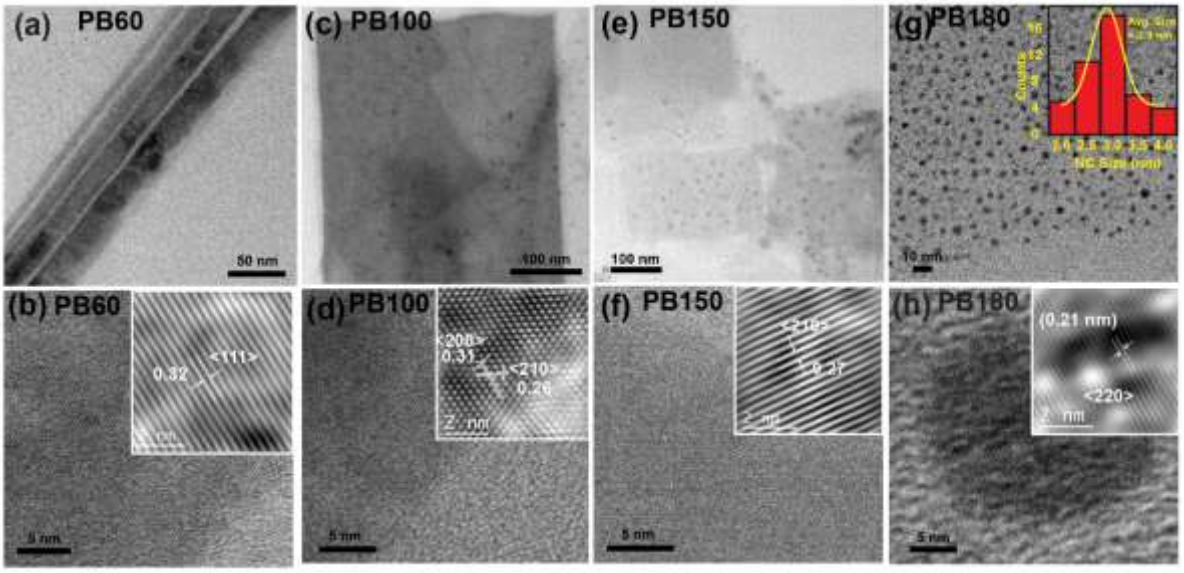

Figure 1: (a,b) TEM image of self-assembled 2D perovskite NRs in PB60 and the corresponding HRTEM lattice image; the inset in (b) shows the corresponding IFFT image with an interplanar spacing of 0.32 nm. (c,d) The TEM image of 2D perovskite NS in PB100 and the corresponding HRTEM image; the inset shows the corresponding IFFT image. (e,f) TEM images of ultrathin 2D perovskite NS in PB150 and the corresponding HRTEM image; the inset shows the corresponding IFFT image. (g,h) The TEM image of 2D perovskite QDs in PB180 and the HRTEM lattice image of a 2D QD. The insets of (g,h) show the size distribution QDs in PB180 and IFFT image of the lattice fringe, respectively.

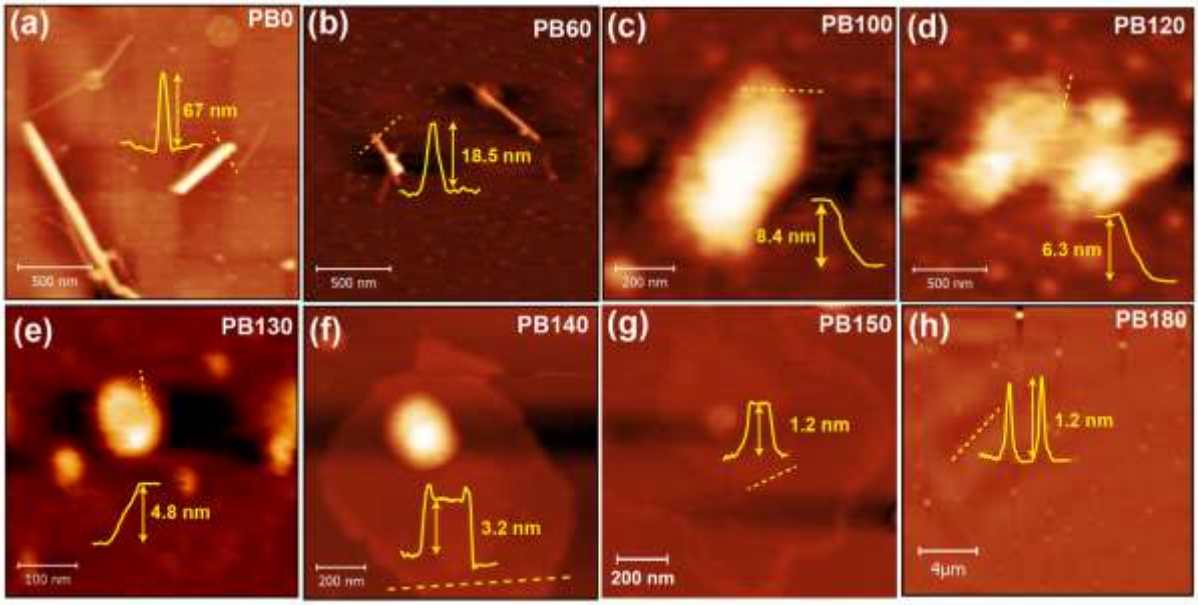

Figure 2: AFM topography images of 2D NS in (a) PB0, (b) PB60, (c) PB100, (d) PB120, (e) PB130, (f) PB140, (g) PB150, and (h) PB180. The corresponding height profiles of the 2D NS are shown in the respective images, which essentially represent the thickness of the 2D layers in each case.

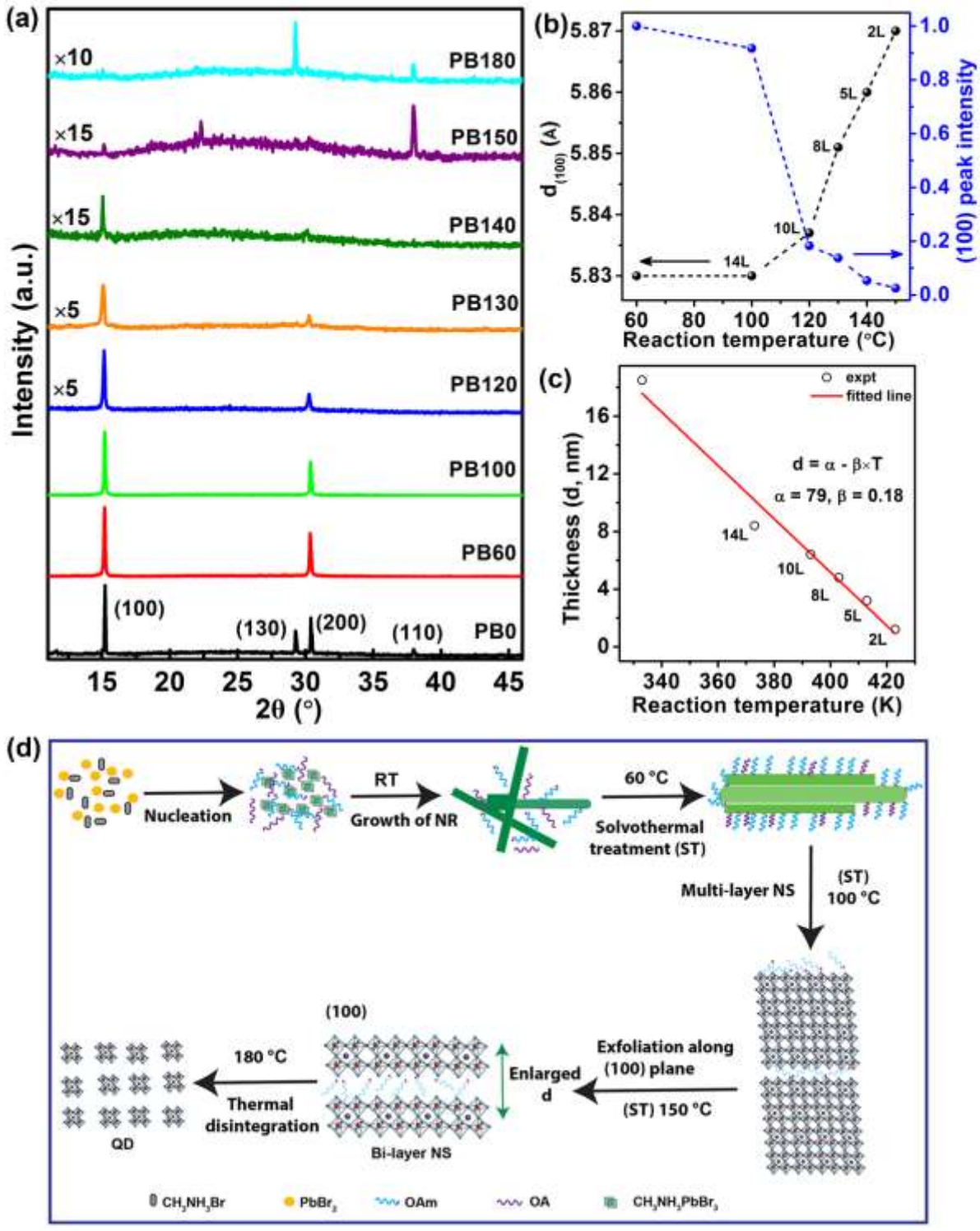

Figure 3: (a) A comparison of XRD patterns of perovskite NS prepared at different solvothermal temperatures. (b) Change in (100) interplanar spacing and (100) peak intensity with solvothermal temperature. (c) Change in the thickness of the 2D NS with solvothermal reaction temperature. (d) A schematic illustration of the growth mechanism and shape evolution of the perovskite NSs during different stages of solvothermal reaction at different temperatures.

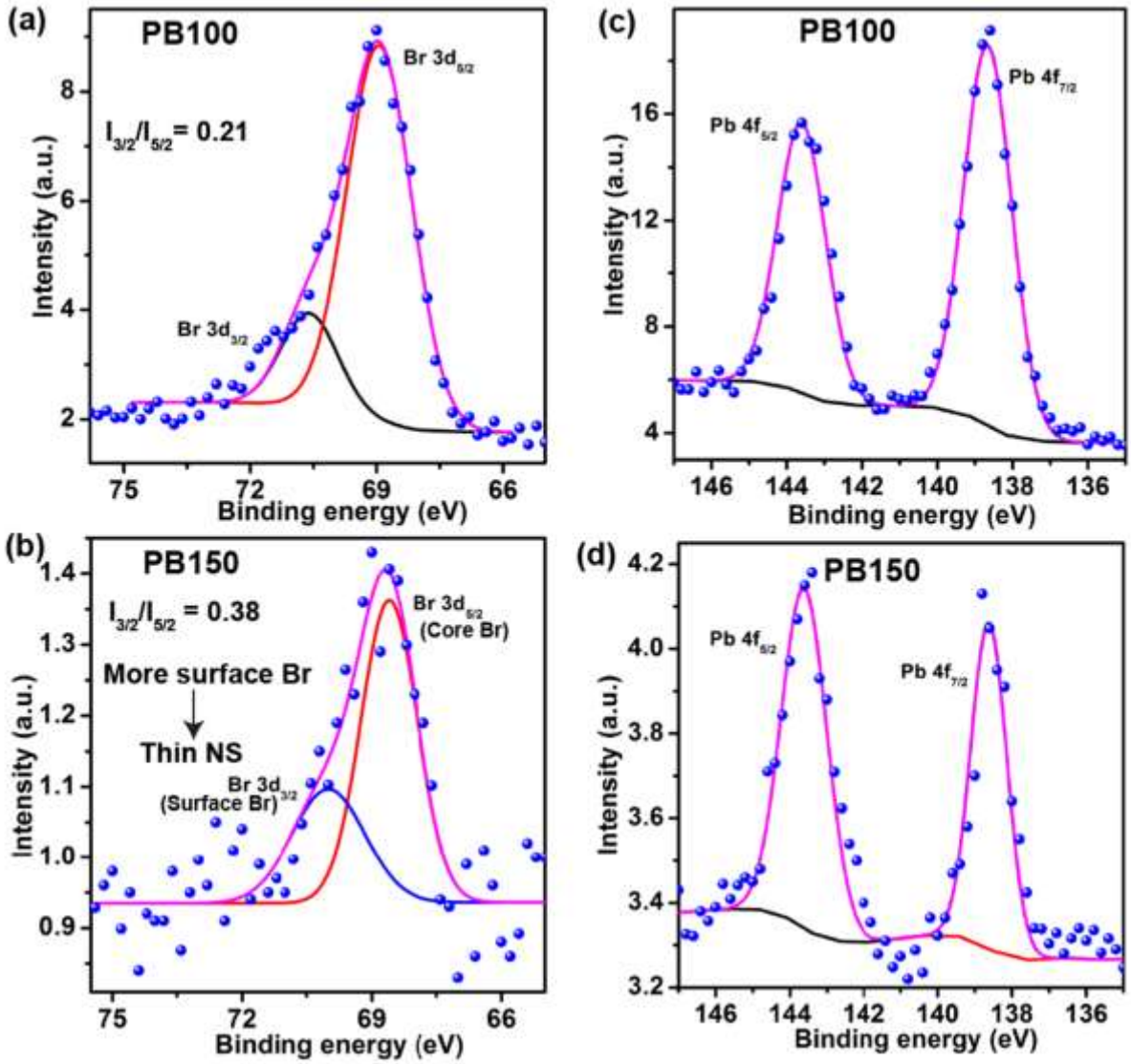

Figure 4: Deconvolution of the XPS spectra corresponding to Br 3d in (a) PB100, (b) PB150. Deconvolution of the XPS spectra corresponding to Pb 4f in (c) PB100, (d) PB150, considering a Shirley background.

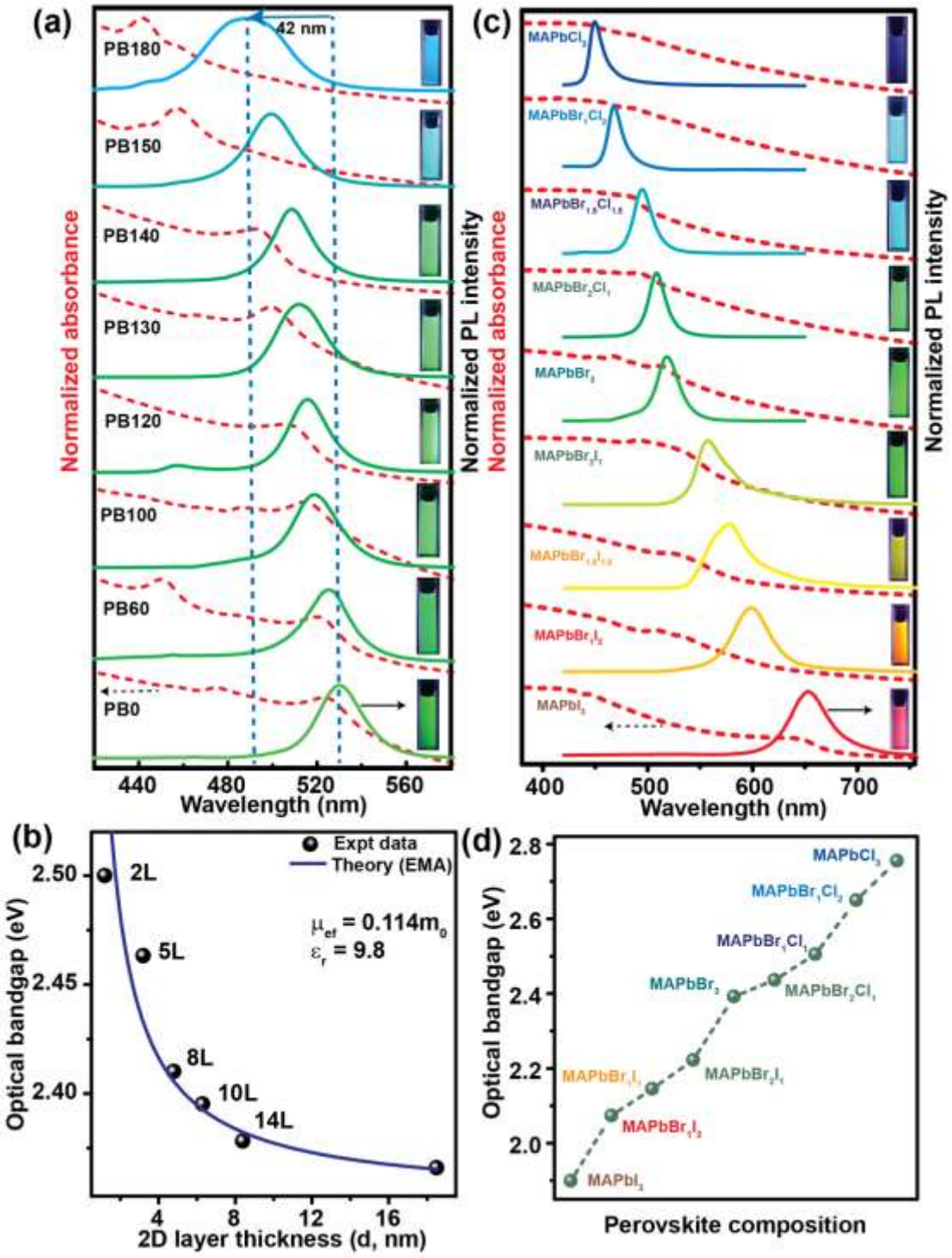

Figure 5: (a) UV-Vis absorption (dashed lines) and PL spectra (solid lines) of various perovskite NSs; the inset in each case shows the corresponding photograph of the sample under UV light irradiation. (b) Variation of the optical bandgap as a function of the thickness of 2D layers. The experimental data are fitted with the quantum confinement model. The data points labeled with xL, where x represents the number of layers. (c) UV-Vis absorption and PL emission spectra of pure and mixed halide perovskite NSs for PB100 obtained by anion exchange. (d) Variation of optical bandgap with halide exchange of multilayered perovskite NS.

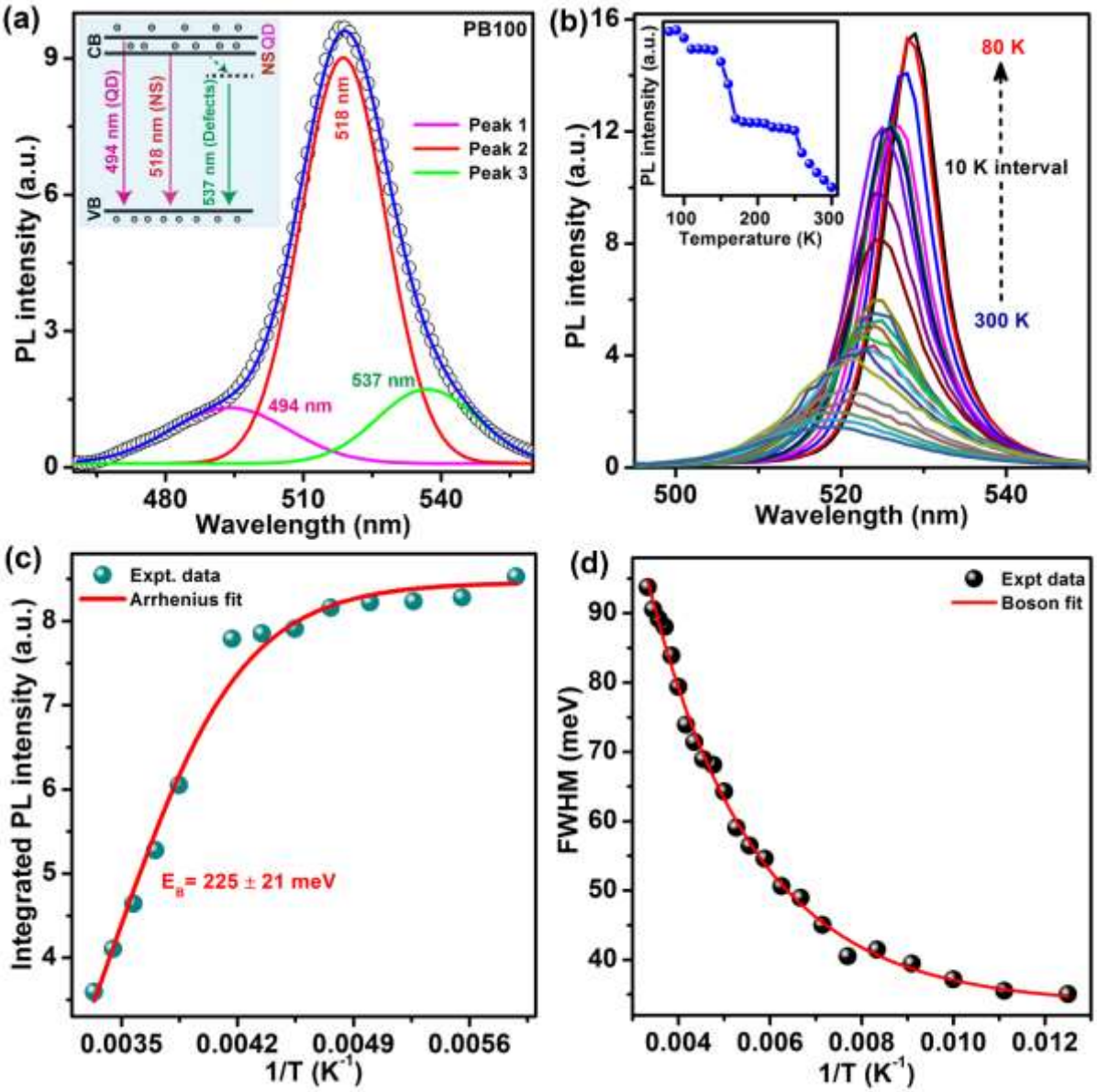

Figure 6: (a) Deconvulated PL spectra of PB100 NS and inset showing band diagram corresponding to each PL peak. (b) Temperature-dependent PL spectra of 2D NS in PB100 in the range 80 K- 300 K. The inset shows the variation of PL intensity with measurement temperature (T). (c) Integrated PL intensity vs. inverse of temperature for PB100. The experimental data are fitted with the Arrhenius equation. (d) Variation of FWHM of PB100 with temperature and the data are fitted with Boson model.

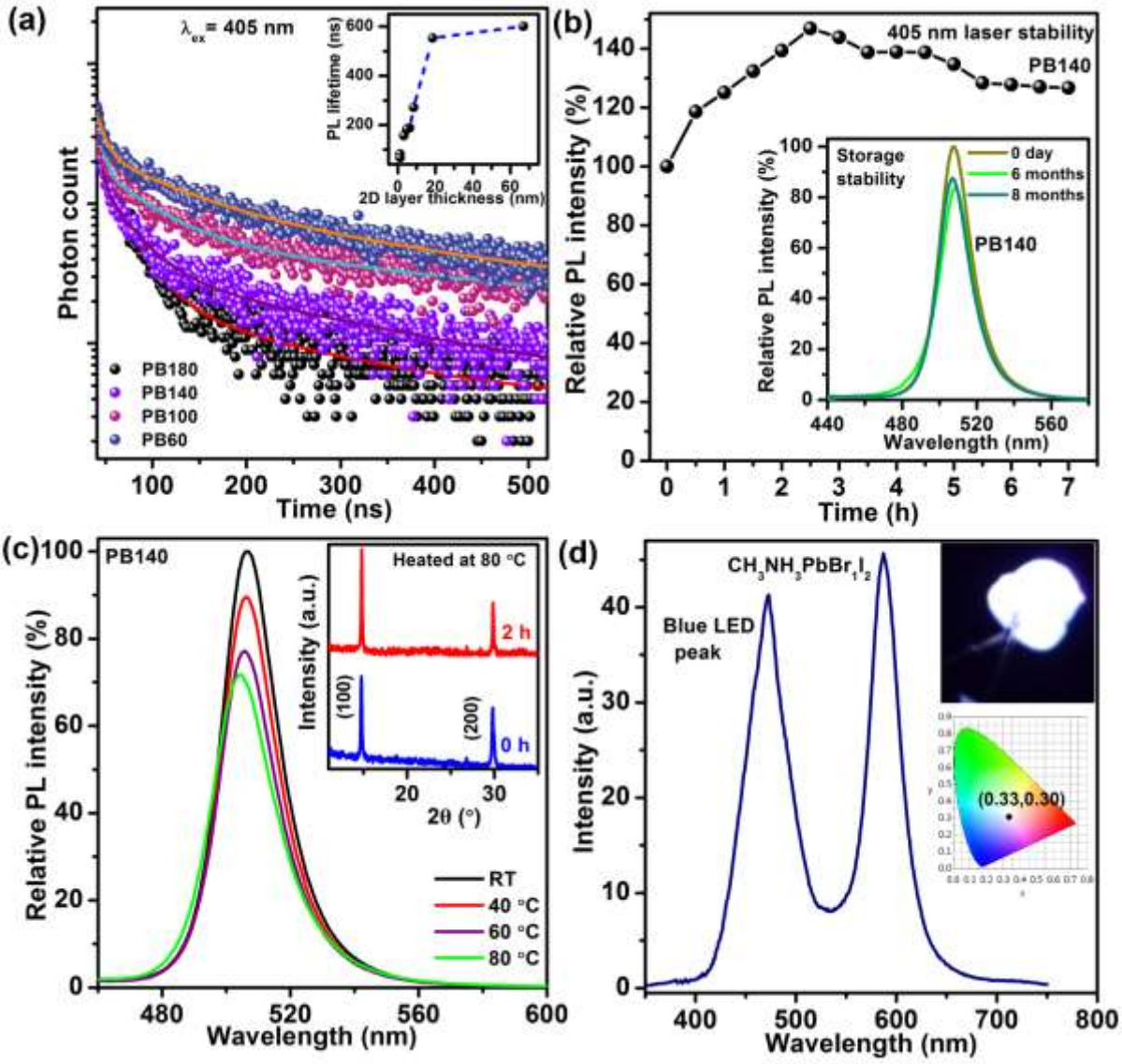

Figure 7: (a) A comparison of TRPL spectra of various 2D perovskite NS (PB60-PB180); the symbols corresponds to experimental data and the solid lines correspond to the fitted data. The inset shows the variation of the PL lifetime with 2D layer thickness. (b) Variation of PL intensity for PB140 as a function of laser (CW) irradiation time; the inset shows the minor change in PL intensity after 8 months storage with respect to that of the freshly prepared sample. (c) Temperature dependent stability of PL emission in PB140. The inset shows the comparison of XRD pattern of PB140 before and after heating at 80 ºC for 2 h. (d) EL spectra of white light-emitting NS device fabricated with blue LED chip and $MAPbBr_1I_2$ NSs. The upper inset shows a digital photograph of the emitting device and the lower inset shown the CIE chromaticity coordinates of the white LED device.

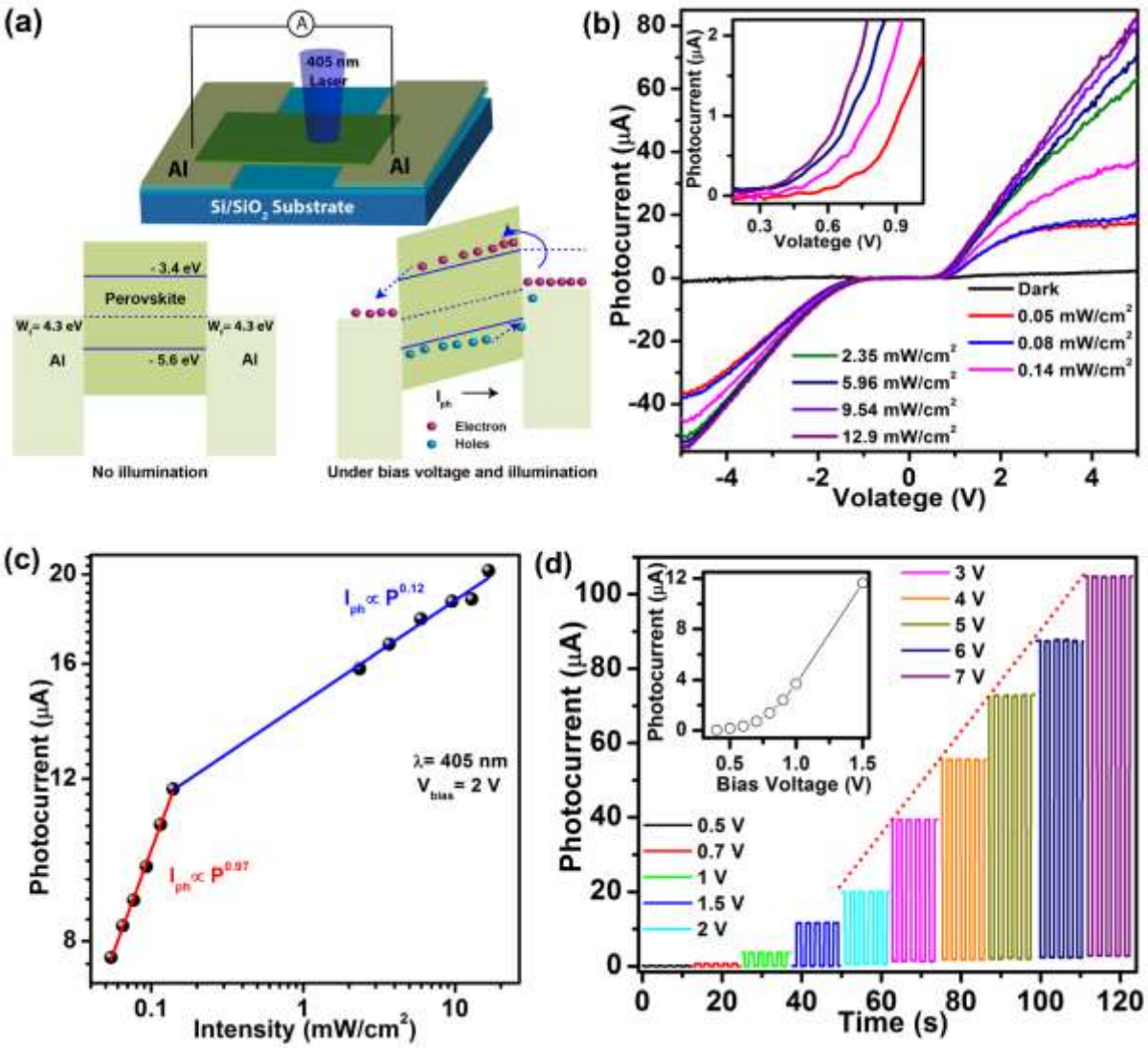

Figure 8: (a) Schematic diagram of a photodetector device fabricated with PB140 NS and the energy band diagram of the Al/$MAPbBr_3$/Al structure before light illumination (no bias) and after light illumination (under bias). (b) I–V characteristics of the photodetector in the dark and under illumination with 405 nm laser for different light irradiation intensities; the inset shows the magnified I–V curve at lower bias voltages. (c) Logarithmic plot of the photocurrent as a function of the light intensity at a bias voltage of 2 V and the data are fitted with a power law. (d) Time-dependent photoresponse of PB140 NS under 405 nm light illumination (5.96 mW/cm^2) recorded at different bias voltages. The inset shows the photocurrent vs. bias voltage for a fixed intensity of illumination.

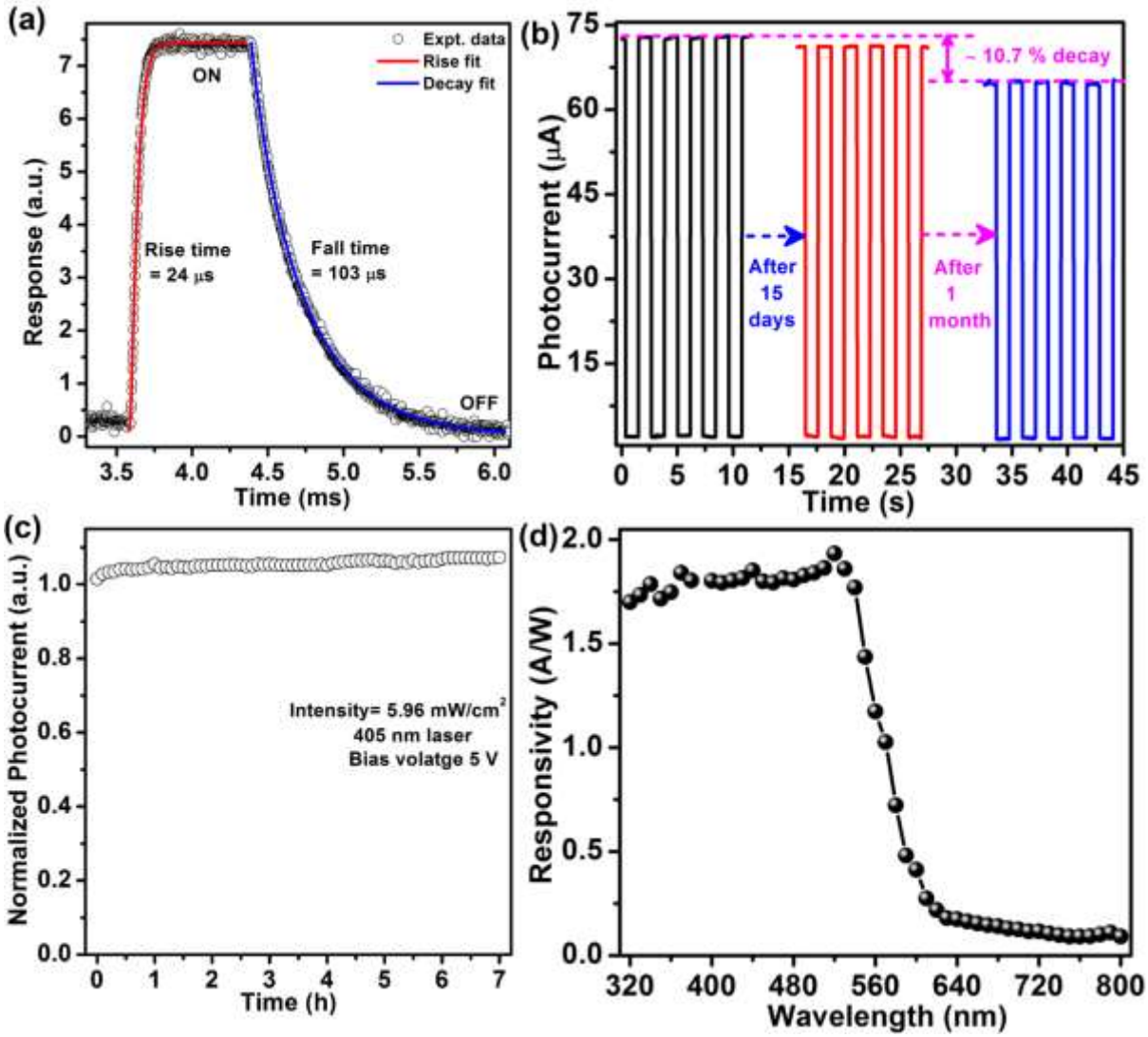

Figure 9: (a) Temporal response of the photocurrent for PB140 NS photodetector measured at a bias of 5 V along with the exponential fits. (b) Photoresponse curve of PB140 NS photodetector device after long-term storage in humid ambient. (c) Normalized photocurrent of PB140 NS photodetector (without encapsulation) with operation time at a bias voltage of 5 V. (d) Spectral responsivity of the NS photodetector recorded at 5 V bias.

Graphical Abstract